SUPERNOVA FEEDBACK EFFICIENCY AND MASS LOADING IN THE STARBURST AND GALACTIC SUPERWIND EXEMPLAR M82

David K. Strickland[1] and Timothy M. Heckman[1]
Accepted for publication in the Astrophysical Journal

ABSTRACT

We measure the net energy efficiency of supernova and stellar wind feedback in the starburst galaxy M82 and the degree of mass-loading of the hot gas piston driving its superwind by comparing a large suite of 1 and 2-dimensional hydrodynamical models to a set of observational constraints derived from hard X-ray observations of the starburst region (the fluxes of the Heα and Lyα-like lines of S, Ar, Ca and Fe, along with the total diffuse $E = 2 - 8$ keV X-ray luminosity). These are the first direct measurements of the feedback efficiency and mass-loading of supernova heated and enriched plasma in a starburst galaxy. We consider a broad range of plausible parameters for the M82 starburst, varying the age and mode of star formation, the starburst region size and geometry, and supernova metal yields. Over all these varied input parameters all the models that satisfy the existing observational constraints have medium to high thermalization efficiencies (30% $\leq \epsilon \leq$ 100%) and the volume-filling wind fluid that flows out of the starburst region is only mildly centrally mass loaded ($1.0 \leq \beta \leq 2.8$). These results imply a temperature of the plasma within the starburst region in the range 30 – 80 million Kelvin, a mass flow rate of the wind fluid out of the starburst region of $\dot{M}_{\rm tot} \sim 1.4 - 3.6 \, M_\odot \, {\rm yr}^{-1}$ and a terminal velocity of the wind in the range $v_\infty = 1410 - 2240 \, {\rm km \, s}^{-1}$. This velocity is considerably larger than the escape velocity from M82 ($v_{\rm esc} \lesssim 460 \, {\rm km \, s}^{-1}$) and the velocity of the Hα emitting clumps and filaments within M82's wind ($v_{\rm H\alpha} \sim 600 \, {\rm km \, s}^{-1}$). Drawing on these results we provide a prescription for implementing starburst-driven superwinds in cosmological models of galaxy formation and evolution that more accurately represents the energetics of the hot metal-enriched phases than the existing recipes do.

Subject headings: ISM: bubbles — galaxies: individual : NGC 3034 (M82) — galaxies: halos — (galaxies:) intergalactic medium — galaxies: starburst — X-rays: galaxies

1. INTRODUCTION

The presence of metals in the intergalactic medium (IGM) at all red-shifts (Songaila 1997), the present-day galaxy mass-metallicity relationship (Garnett 2002; Tremonti et al. 2004), and $\sim$ 100-kpc-scale holes in the IGM at red-shift $z \sim 3$ (Adelberger et al. 2003) have all been interpreted as the consequence of energetic metal-bearing outflows from galaxies.

There is no doubt that at least one form of galactic wind exists: starburst galaxies are commonly observed to host supernova-driven galactic-scale winds (Heckman et al. 1990; Heckman 2003) in both the local and high redshift Universe (Lehnert & Heckman 1996a; Pettini et al. 2001; Shapley et al. 2003). These superwinds are phenomenologically complex and are comprised of multiple different gas phases moving at different velocities (Bland-Hawthorn 1995; Dahlem 1997; Heckman et al. 2000, 2001; Veilleux et al. 2005). However, the very hot plasma long hypothesized to be the prime mover in superwinds (Chevalier & Clegg 1985), often called the wind fluid, has only recently been directly observed in the archetypal superwind associated with the starburst galaxy M82 (Griffiths et al. 2000; Strickland & Heckman 2007).

The most fundamental long-standing uncertainty in our understanding of the nature of superwinds and their larger scale role is the value of the energy per particle of the metal-enriched wind-fluid that drives an individual superwind. Both supernovae (SNe) and stellar winds from massive stars are responsible for supplying the kinetic energy that drive superwinds (Stellar winds only contribute $\sim$ 10% of the total mechanical power of a starburst, but they may supply up to half of the gas mass returned to the ISM, see Leitherer et al. 1992;

Leitherer & Heckman 1995). What fraction of the $\sim 10^{51}$ erg of kinetic energy released per star that ultimately goes supernova is actually available to drive bulk motions of the ISM? As it is understood that SNe dominate the energy return this is often termed the SN thermalization efficiency or the SN feedback efficiency, even though stellar winds do play some small part energetically. Is the metal-enriched mix of SN and stellar wind ejecta diluted and cooled by mixing with the ambient ISM, i.e. is the wind-fluid mass-loaded? If this ejecta is to escape the galaxy and enter the IGM then its specific energy must exceed its initial gravitational potential energy, and furthermore the total energy in the wind-fluid must be sufficient to perform the mechanical work necessary to move the interstellar and halo gas that lies between the starburst region and the IGM (Mac Low & McCray 1988; Strickland et al. 2004b).

For moderate to high thermalization efficiency (efficiencies $\gtrsim$ 10%), the wind-fluid is expected to have an initial temperature within the starburst region in the range 10 – 100 million Kelvin (Chevalier & Clegg 1985), even if it has been lightly mass-loaded with cold ambient gas. Such temperatures are far hotter than the neutral, warm ionized or soft X-ray emitting plasmas that are the most easily observed phases within superwinds (Dahlem 1997; Veilleux et al. 2005).

However it has only recently become technically possible to detect the diffuse hard X-ray emission that would be associated with a plasma in the temperature range $10^7 \lesssim \log T$ (K) $\lesssim 10^8$. The starburst regions of even the nearest starburst galaxies only subtend $\sim 15 - 45''$ on the sky and are heavily populated with X-ray-luminous compact objects. It was only with the advent of $\sim 1''$-spatial resolution X-ray astronomy in 1999 following the launch of the *Chandra* X-ray Observatory that made it possible for Griffiths et al. (2000) to resolve out

[1] Department of Physics and Astronomy, The Johns Hopkins University, 3400 N. Charles St., Baltimore, MD 21218, USA.

the point source emission in the archetypal nearby starburst galaxy M82 and reveal residual diffuse hard X-ray emission, although of uncertain origin.

It is important to distinguish between the material that actually drives a superwind, and the other more easily observed phases of swept-up and entrained gas that are part of the wind. We define the wind-fluid as the material whose high thermal and/or ram pressure drives the superwind. The wind fluid certainly comprises a significant fraction of the merged SN ejecta and massive star stellar wind material, probably admixed (mass-loaded[2]) with some ambient gas from with starburst region.

Although other gas phases may dominate the total gas mass budget of a superwind, they are less important with respect to the issue of energy and metal transfer into the IGM. Furthermore the ejection of these phases is less than certain, as the measured warm neutral and warm ionized medium (WNM, WIM) gas velocities are typically comparable to the galactic escape velocities (Heckman et al. 2000; Martin 2005; Rupke et al. 2005). Unfortunately even the most recent attempts to include superwinds in cosmological models of galaxy formation use only simplified single-phase winds, often with energetics and masses based on the observed WNM/WIM properties of superwinds (see e.g. Springel & Hernquist 2003a; Bertone et al. 2005). These models do not properly address the physics of hot-phase metal transport in addition to having overly low values of the energy per particle, which casts the reliability of their conclusions into doubt.

Attempts have been made to use measurements of the temperature of the extended soft X-ray emitting plasmas ($T \sim 2 - 7 \times 10^6$ K) in starburst galaxies to constrain whether the hot gas will escape the host galaxy (see e.g. Martin 1999), but such an approach neglects both the significant kinetic energy expected to be associated with this material and that the soft X-ray emitting plasma is an indirect probe of the properties of the true wind-fluid (Strickland & Stevens 2000).

The detection of apparently thermal diffuse hard X-ray emission of temperature $\sim 4 \times 10^7$ K in the starburst region of M82 in the 33 ks-long *Chandra* ACIS-I observations of Griffiths et al. (2000) suggested it was possible to directly observe and constrain the properties of the wind fluid in a starburst superwind.

We recently obtained and analyzed a new 18 ks *Chandra* ACIS-S observation of M82, and also reprocessed archival

---

[2] We will use the term mass loading to denote the addition and efficient mixing of ambient ISM into the full volume of the wind-fluid, which is consistent with the terminology in Suchkov et al. (1996). Technically mass loading need not affect the entire flow and can be localized, see e.g. Dyson et al. (1993). Furthermore the form of mass-loading considered in this work occurs only within the starburst region itself ("centralized mass loading") although ultimately it affects the entire flow. We find it conceptually beneficial to differentiate between *mass loading* and *entrainment* in superwinds. Mass loading affects the density of one gaseous phase by mixing in material from another phase, almost always a cooler and denser phase. The origin and fate of the secondary phase is unimportant given the focus on the properties of the primary phase. Entrainment is the incorporation into the superwind of subsidiary gas phases that leads to creating or sustaining a multiphase superwind. The entrained material is usually ambient disk or halo gas over-run or swept-up by the wind fluid, and retains much of its original character, albeit with some modification. Although entrainment processes may lead to mass loading of the wind fluid the two processes are not synonymous. In principle entrainment could occur without leading to significant mass loading of the wind fluid. One can not realistically hope to represent or approximate the totality of a multiphase superwind as a single phase mass loaded flow. Only specific components of the superwind are amenable to such treatment, of which the wind fluid is the clearest example.

Chandra ACIS-I and *XMM-Newton* observations[3] (total exposure of 48 ks with ACIS-I, 75 ks with *XMM-Newton* PN and 102 ks with each MOS instrument). We confirmed the presence of both diffuse continuum and diffuse $E \sim 6.7$ keV Fe Heα line emission within the central starburst region (Strickland & Heckman 2007, hence forth referred to as Paper I). Having assumed that the line-emitting plasma is metal-enriched to $Z_{\rm Fe} \sim 5 Z_{\rm Fe,\odot}$, we found that the observed iron line luminosity of $L_{X,6.7} \sim (1.1 - 1.7) \times 10^{38}$ erg s^{-1} was consistent with the properties of the wind fluid expected given M82's star formation rate, provided that the SN thermalization efficiency was high. However the diffuse hard X-ray continuum luminosity of $L_{X,2-8} \sim 4.4 \times 10^{39}$ erg s^{-1} was too luminous to be the thermal bremsstrahlung associated with the wind fluid given the parameters assumed when interpreting the iron line emission.

In this paper we consider in greater detail what constraints the observed hard X-ray properties of M82 can place on the properties on the superwind and the wind-fluid, in particular the efficiency of SN heating (ϵ) and the degree of central mass-loading (β). Ultimately these determine the energy per particle of the wind fluid. We restrict analysis to the starburst region within $r \sim 500$ pc of the center of M82. We calculate the X-ray emission using both multi-dimensional hydrodynamical simulations and the 1-dimensional analytical Chevalier & Clegg (1985) model (hence forth referred to as the CC model). By using the simple but relatively accurate CC model we can explore the predicted X-ray properties of the wind fluid in models covering a wider range of parameter space than if we used multi-dimensional hydrodynamical simulations alone.

A variety of recent papers have presented theoretical calculations of the broad-band X-ray emission from individual star-forming clusters, using either the adiabatic CC model, or the non-adiabatic solution of Silich and collaborators (Cantó et al. 2000; Stevens & Hartwell 2003; Oskinova 2005; Silich et al. 2005; Ji et al. 2006), with the aim of seeing if the particular model used can explain the observed data. Our motivation differs from these papers, in that our aim is to use theoretical models in combination with observational data on M82 to constrain fundamental properties of the superwind. In addition our approach differs from these previous papers in its use of X-ray line luminosities rather than purely broad-band X-ray luminosities. In reality the broad-band emission might be dominated by non-thermal continuum sources. Furthermore line emission is more sensitive than the thermal continuum luminosity to interesting parameters such as the plasma temperature.

2. OBSERVATIONAL CONSTRAINTS ON HIGH TEMPERATURE GAS IN M82

The observational constraints derived in Paper I on the diffuse hard X-ray emission within $r = 500$ pc of the nucleus of M82 from the *Chandra* and *XMM-Newton* observations are summarized in Table 1. These comprise a robust 6.69 keV iron line detection ($> 4\sigma$ in significance), an upper limit on the 6.96 keV iron line, and from the *Chandra* observations the luminosity of the diffuse continuum. For the *Chandra*-based observations the values refer to the diffuse emission alone, after the exclusion of detected point-like X-ray sources and corrections for undetected point sources based on the observed

---

[3] *Chandra* ObsId numbers 2933, 361 and 1302. The *XMM-Newton* data ObsIds are 0112290201 and 0206080101.
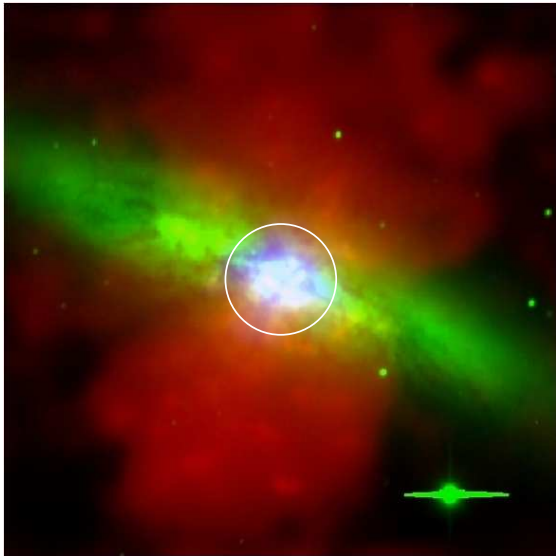
FIG. 1.— A three color composite image of M82 showing the region within a 500 pc radius of the nucleus (white circle) in comparison to the galaxy and superwind. Soft X-ray emission in the 0.3–2.8 keV energy band is shown in red, optical R-band emission (starlight) in green, and diffuse hard X-ray emission in the 3 – 7 keV energy band in blue. The X-ray images are adaptively smoothed Chandra ACIS-S images with point source emission removed and interpolated over. The image is $4'.8$ (~ 5 kpc) on a side.

point source luminosity function. These luminosities also include 32% and 20% upward corrections to the luminosities derived from the ACIS-S and ACIS-I data to account for regions excluded from the spectra due to remove the emission from detected point sources. For the *XMM-Newton* observation the line luminosities include all emission within $r = 500$ pc, but the contribution to the line luminosities from point-like sources is expected to be small in this particular observation.

Note that the region of bright diffuse hard X-ray emission studied in this paper is associated with the nuclear starburst region. As can be seen from Fig. 1 this region is much smaller than the full 12-kpc-scale superwind that is most often studied in optical (Lehnert et al. 1999) or soft X-ray emission (Stevens et al. 2003).

As discussed in Paper I the nature of the diffuse broad-band continuum is not clear. If the continuum is thermal then the relative strength of the iron line emission to the observed continuum is much lower than expected for a plasma of Solar elemental abundances, let alone the iron-enriched plasma expected from recent core-collapse SNe. We demonstrated that a wind mass-loaded with additional ambient gas could produce the total broad-band X-ray luminosity that we observe, but the required degree of mass loading could not sufficiently reduce the relative strength of the iron line to the continuum. Thus the best fit bremsstrahlung models for the continuum do not necessarily provide meaningful estimates of the temperature of the iron-emitting plasma, and should be interpreted with caution. Power law spectral models provide a marginally better fit to the continuum than do thermal bremsstrahlung models. Thus a non-thermal process such as Inverse Compton X-ray emission might be responsible for the majority of the diffuse hard X-ray continuum. The X-ray luminosity associated with Inverse Compton emission depends sensitively on the unknown magnetic field strength within the starburst region. In Paper I we estimated it might account for $\sim 25\%$ of the observed diffuse X-ray luminosity in the $E = 2 - 8$ keV energy band, although other authors have in the past given

higher luminosity estimates for Inverse Compton emission from M82 (Schaaf et al. 1989; Moran & Lehnert 1997).

The upper limits on the iron 6.96 keV / 6.69 keV line flux ratio[4] of < 0.34 place upper limits on the temperature of $T < 7.8 \times 10^7$K if the plasma is in collisional equilibrium (see Table 2). The Coulomb relaxation and ionization equilibrium timescales presented in Paper I are much shorter than the timescale for plasma to flow out of the starburst region, so the assumption of collisional ionization equilibrium is reasonable.

Other lines in the $2 \leq E$ (keV) ≤ 10 hard X-ray band may in principle be used to constrain the plasma temperature in a starburst region. In particular the helium-like and hydrogen-like ions of sulphur (at $E \sim 2.45$ keV and $E \sim 2.62$ keV respectively), argon ($E \sim 3.13$ keV and $E \sim 3.33$ keV) and calcium ($E \sim 3.90$ keV and $E \sim 4.11$ keV) can be detected in CCD spectra from the *Chandra* ACIS and *XMM-Newton* EPIC instruments. These lines are most intense in plasmas with temperatures in the range $\log T \sim 7.0 - 7.5$, somewhat lower than the optimal temperature for the iron lines, but this might be advantageous in diagnosing starbursts where mass loading is significant and/or the efficiency of SN thermalization is low.

In Paper I we specifically excluded data at the expected energies of the S, Ar and Ca lines from the fitting of the M82 nuclear region spectra. Repeating the analysis described Paper I but now fitting all the data in the energy range $E = 2.2 - 9.0$ keV in both the *XMM-Newton* and *Chandra* ACIS-S spectra yields the line detection significances and line luminosities given in Table 3. We fit for the intensity of the helium-like and hydrogen-like S, Ar and Ca lines, having fixed the line energies at the expected values. These lines are faint, but in some cases likely to be real. As an example we display the best-fit to the *XMM-Newton* EPIC pn + MOS spectra in Fig. 2. Detection significance was assessed using Monte Carlo methods with several thousand simulated spectra. Where the line detection significance was $< 3\sigma$ we give the 99% upper limit on the line luminosity (and not the best-fit value). The *Chandra* ACIS-I spectra gave similar results to those from ACIS-S, but as the line detections are less significant than in the *XMM-Newton* data there is little reason to present the values.

In the *XMM-Newton* EPIC pn + MOS spectra of M82's nucleus the equivalent of the Heα line from highly ionized S, Ar, Ca and Fe are all detected with significances $\gtrsim 3\sigma$, while in the shorter (and hence lower S/N) *Chandra* ACIS-S spectrum of the nuclear diffuse emission the S Heα and Fe Heα are detected at $\gtrsim 3\sigma$ while the Ar Heα and Ca Heα lines are only detected at $\lesssim 2\sigma$. In both instruments Si Lyβ is also detected at high significance, but we shall ignore this lower ionization state line in the analysis to follow. The only Lyα-like line detected at $\gtrsim 3\sigma$ is S Lyα in the *XMM-Newton* EPIC spectra.

Using the robust line detections (i.e. those with significance $\geq 3\sigma$) we can estimate the plasma temperature from the ratio of S Lyα to S Heα, and from between different elements from the ratio of the various Heα lines (assuming their relative elemental abundances are Solar). These temperature estimates are presented in Table 2. The S ions tightly constrain the ion temperature to $\log T \approx 7.1$, while the ratio of the S, Ar or Ca Heα line to the Fe Heα line yields $\log T \sim 7.3$. The ratio of S Heα to either Ar Heα or Ca Heα yields a temperature estimate of $\log T \sim 7.2$.

This pattern of the inferred temperature increasing as higher

---

[4] Note that the line ratios quoted in Paper I were the ratio of the photon fluxes, whereas in this paper we quote the energy flux ratio.

TABLE 1
DIFFUSE CONTINUUM AND IRON LINE LUMINOSITIES FROM PAPER 1.

Instrument (1)	ObsID (2)	$\log L_{2-8keV}$ (3)	$\log L_{FeK\alpha}$ (4)	$\log L_{FeHe\alpha}$ (5)	$\log L_{FeLy\alpha}$ (6)
XMM-Newton EPIC	0206080101	$\cdots$	$37.31^{+0.23}_{-0.54}$	$38.13^{+0.05}_{-0.06}$	< 37.66
Chandra ACIS-S	2933	$39.65^{+0.02}_{-0.05}$	$37.94^{+0.22}_{-0.48}$	$38.23^{+0.16}_{-0.27}$	< 38.15
Chandra ACIS-I	361+1302	$39.64^{+0.02}_{-0.02}$	$37.93^{+0.20}_{-0.26}$	$38.13^{+0.14}_{-0.25}$	< 38.01

NOTE. — This table summarizes the results presented in Strickland & Heckman (2007) on the emission from within $r = 500$ pc of the nucleus of M82. Column 2: The ObsID is the identification number allocated to each observation by the *Chandra* and *XMM-Newton* Science Centers. Column 3: Logarithm of the total diffuse X-ray luminosity in the $E = 2 - 8$ keV energy band, including line emission. Column 4: Logarithm of the $E \sim 6.4$ keV Fe Kα line luminosity. Column 5: Logarithm of the $E \sim 6.7$ keV Fe Heα line luminosity. Column 6: Logarithm of the $E \sim 6.96$ keV Fe Lyα line luminosity. The quoted uncertainties are 68.3% confidence for one interesting parameter, while the upper limits are 99.0% confidence.

TABLE 2
TEMPERATURE ESTIMATES FOR THE DIFFUSE HARD X-RAY EMISSION.

Basis for temperature estimate (1)	Detector (2)	$\log T$ (K) (3)
Fe Lyα / Fe Heα	XMM-Newton	< 7.89
Fe Lyα / Fe Heα	ACIS-S	< 8.05
Fe Lyα / Fe Heα	ACIS-I	< 8.04
Ca Heα / Fe Heα	XMM-Newton	$7.31^{+0.10}_{-0.06}$
Ca Heα / Fe Heα	ACIS-S	> 7.21
Ar Heα / Fe Heα	XMM-Newton	7.30 ± 0.03
Ar Heα / Fe Heα	ACIS-S	> 7.29
S Heα / Fe Heα	XMM-Newton	7.26 ± 0.01
S Heα / Fe Heα	ACIS-S	$7.23^{+0.06}_{-0.03}$
(Ca Lyα + Ca Heα) / Fe Heα	XMM-Newton	> 7.22
(Ca Lyα + Ca Heα) / Fe Heα	ACIS-S	> 7.12
(Ar Lyα + Ar Heα) / Fe Heα	XMM-Newton	> 7.26
(Ar Lyα + Ar Heα) / Fe Heα	ACIS-S	> 7.20
(S Lyα + S Heα) / Fe Heα	XMM-Newton	$7.30^{+0.01}_{-0.02}$
(S Lyα + S Heα) / Fe Heα	ACIS-S	> 7.26
S Heα / Ca Heα	XMM-Newton	$7.22^{+0.07}_{-0.05}$
S Heα / Ca Heα	ACIS-S	< 7.27
S Heα / Ar Heα	XMM-Newton	7.19 ± 0.05
S Heα / Ar Heα	ACIS-S	< 7.11
Ar Heα / Ca Heα	XMM-Newton	$7.28^{+0.13}_{-0.16}$
Ca Lyα / Ca Heα	XMM-Newton	< 7.63
Ca Lyα / Ca Heα	ACIS-S	< 7.69
Ar Lyα / Ar Heα	XMM-Newton	< 7.42
Ar Lyα / Ar Heα	ACIS-S	< 7.59
S Lyα / S Heα	XMM-Newton	$7.10^{+0.02}_{-0.04}$
S Lyα / S Heα	ACIS-S	< 7.12
Bremsstrahlung fit to diffuse continuum	ACIS-S	$7.64^{+0.22}_{-0.16}$
Bremsstrahlung fit to diffuse continuum	ACIS-I	$7.50^{+0.09}_{-0.07}$

NOTE. — Temperature estimates are given only for line ratios where one or more of the lines involved is detected at $\geq 3\sigma$. The quoted uncertainties are 68.3% confidence for one interesting parameter, while both upper and lower limits are 99.0% confidence.

ionization state ions are used (which are of course more sensitive to higher temperatures) indicates that either the plasma is multi-phase, and/or the the plasma is not in collisional ionization equilibrium (CIE). Of these explanations we favor the former, as multi-dimensional numerical hydrodynamical simulations predict a broad range of gas temperatures below $\log T \sim 8$ (see e.g. Strickland & Stevens 2000). Furthermore we discussed in Paper I reasons to expect the Fe-emitting plasma to be in or close to CIE.

Unfortunately these results do not strongly constrain the temperature of the Fe-emitting plasma. One possibility is that the iron line emission arises in the very hottest phases in the superwind, i.e. at $\log T \lesssim 7.9$, and that most of the S, Ar and Ca emission comes from somewhat cooler components associated with the wind/ISM interaction and the larger scale soft X-ray emission in the M82 superwind. In this case, given the possible soft X-ray contribution, the S, Ar and Ca observed luminosities must be treated as upper limits to the S, Ar and Ca line emission coming from the volume filling wind-fluid. Alternatively the wind fluid is relatively cool, with a temperature corresponding to that measured from the Ar and Ca lines, i.e. $\log T \sim 7.3$, and the Fe lines are produced by some unexplained non-thermal mechanism.

In either case a successful model of M82's nuclear emission must reproduce the observed hard X-ray iron line emission without over-producing the broad-band continuum and S, Ar
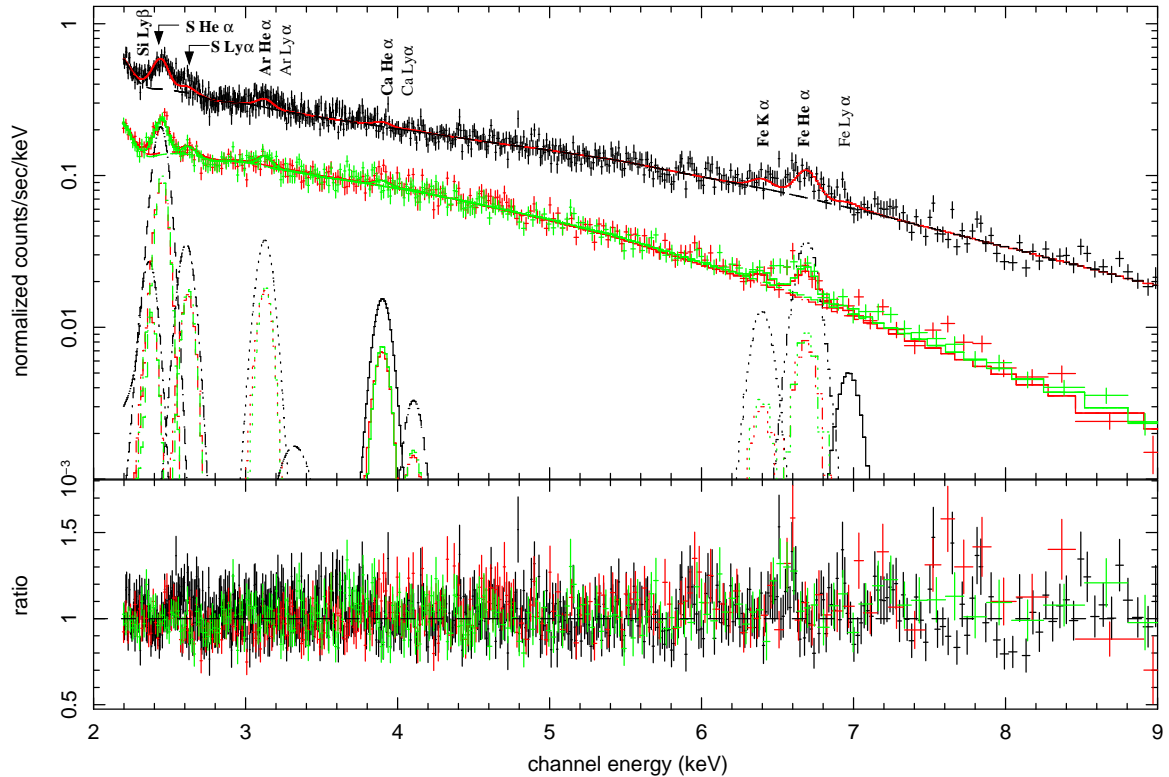
Fig. 2.— (Upper panel) The *XMM-Newton* EPIC pn (black data points with error bars), MOS1 (red data points) and MOS2 (green data points) spectra of the central 500 pc of M82. The best-fit spectral model (red solid line) is shown, along with the named X-ray line components of the model (dashed and dotted lines with a color matching the parent data). The Heα-equivalent lines of S, Ar, Ca and Fe, along with Si Lyβ and S Lyα, are all detected with significances of $\gtrsim 3\sigma$. The other lines have lower significance. (Lower panel) The residuals from the best-fit model.

TABLE 3
HARD X-RAY S, AR AND CA LINE DETECTIONS AND LUMINOSITIES IN M82.

Line (1)	Ion (2)	Energy (3)	Detector (4)	Significance (5)	$\log L_X$ (6)
Heα	S XV	2.45	XMM-Newton	> 3.5	38.19 ± 0.02
S Lyα	S XVI	2.62	XMM-Newton	> 3.5	$37.43^{+0.08}_{-0.10}$
Ar Heα	Ar XVII	3.13	XMM-Newton	> 3.5	$37.53^{+0.07}_{-0.08}$
Ar Lyα	Ar XVIII	3.32	XMM-Newton	0.8	< 37.26
Ca Heα	Ca XIX	3.90	XMM-Newton	3.5	$37.27^{+0.12}_{-0.17}$
Ca Lyα	Ca XX	4.11	XMM-Newton	1.1	< 37.14
S Heα	S XV	2.45	ACIS-S	> 3.9	$38.32^{+0.06}_{-0.07}$
S Lyα	S XVI	2.62	ACIS-S	1.7	< 37.64
Ar Heα	Ar XVII	3.13	ACIS-S	1.9	< 37.56
Ar Lyα	Ar XVIII	3.32	ACIS-S	0.5	< 37.69
Ca Heα	Ca XIX	3.90	ACIS-S	2.4	< 37.52
Ca Lyα	Ca XX	4.11	ACIS-S	0.5	< 37.54

NOTE. — The luminosities are given as $\log_{10}$ of the line luminosity in units of erg s^{-1}, assuming a distance to M82 of $D = 3.6$ Mpc and zero intrinsic absorption. Line energies are in units of keV. Line significances are the σ values equivalent to the enclosed probability $1 - p$ for a two-tailed Gaussian, where p is the probability of the line being spurious. In the case of highly significant lines we can only estimate a lower limit to the significance of the line. The quoted uncertainties on the luminosities are 68.3% confidence, while upper limits on $\log L_X$ are provided at 99.0% confidence if the line significance is $< 3\sigma$.

and Ca line emission.

3. THEORETICAL AND NUMERICAL METHODOLOGY

Hard X-ray emission in multi-dimensional hydrodynamical models of superwinds is dominated by the thermal emission from starburst region itself (Tomisaka & Bregman 1993; Suchkov et al. 1994; Strickland & Stevens 2000).

If the starburst region is spherical then the plasma proper-ties of this region obtained from hydrodynamical simulations agree very well with the simple one-dimensional radially-symmetric analytical CC model, in which the mechanical energy and returned gaseous ejecta from core-collapse supernovae are injected at a uniform rate only within a radius $R_\star$, and radiative energy losses are assumed to be negligible. Gravity and any surrounding ambient gaseous medium are ignored.

As the feedback parameters we wish to constrain are related to the observable X-ray emission via the plasma properties in the starburst region it is worthwhile for us to explicitly reproduce the analytical solution obtained by Chevalier & Clegg (1985). We consider the conditions under which the adiabatic assumption inherent in the CC model may be invalid in Appendix A, but we will show that for most reasonable parameters associated with the M82 starburst (described below) the radiative energy losses are not significant.

In real galaxies starburst regions are better described as disks or ring of star-formation rather than spherical regions. To explore the predicted X-ray emission for our default model of the M82's disk-like starburst we begin by using 2-dimensional hydrodynamical simulations in cylindrical symmetry to predict the plasma properties within the a radius of 500 pc of the center of the galaxy.

However, with appropriate scaling (see Appendix B), it is possible to use the 1-dimensional CC model with a spherical starburst to predict the plasma properties of the wind fluid within a non-spherical starburst region to high accuracy, and to predict the hard X-ray emission from even larger regions with an accuracy no worse than the uncertainties in the observed X-ray luminosities.

These scaled CC models are considerably faster to calculate than a full hydrodynamical model, so we will use them to explore how the constraints on the thermalization efficiency and mass loading change if we adopt a different range of parameters for the M82 starburst.

This approach, in particular the use of the scaled CC model, is applicable only to the study of the wind fluid in the vicinity of the starburst region. It is not intended for use as a model of an entire superwind as it neglects the interaction between the wind fluid and the multiphase ambient ISM. The simplification of neglecting the ambient ISM works because the only significant source of thermal hard X-ray emission in a superwind is the wind fluid itself, in particular the wind fluid within the starburst region. The interactions between the wind fluid and the multiphase ISM are important in the large scale wind and for its emission at soft X-ray and longer wavelengths (e.g. Strickland & Stevens 2000; Cooper et al. 2008), but with the exception of altering the net efficiency of SN+SW heating and any mass-loading of the wind fluid these interactions are not expected to alter the properties of the wind fluid within the starburst region to any significant degree given its energetic dominance.

3.1. *2-Dimensional Hydrodynamical Modeling*

The hydrodynamical simulations were performed using the multi-dimensional numerical hydrodynamics code VH-1 (Blondin et al. 1990). Simulations were performed in 2-dimensional cylindrical symmetry with a cell size of 2 pc over 500 by 500 cell computational grid. Reflecting boundary conditions were imposed along the r and z axes, with inflow/outflow boundary conditions are the other edges of the computational grid.

Energy and mass are injected within the starburst region in the manner described in Strickland & Stevens (2000). In general the starburst region was modeled as disk-like region of the size described in § 3.3. No gravitational forces or radiative cooling are considered for the purposes of consistency with the analytical CC model described below.

The computational grid was initially populated with a tenuous ISM of density $\rho = 2 \times 10^{-28} \, \mathrm{g \, cm^{-3}}$ and temperature $T = 8 \times 10^3$ K. The simulations were run until the wind had

blown the initial ISM off the grid and reached a steady-state solution, which typically occurred $t \sim 1 - 2$ Myr after the onset of the simulation. Gas properties and X-ray luminosities are measured at a time of 3 Myr within a spherical region of radius of 500 pc to closely match the observed region discussed in § 2.

3.2. *The 1-Dimensional Analytical CC Solution*

For completeness we present the analytical flow solution derived by CC, and how we use it to derive the fluid properties as a function of radial position. More complicated, but also more generalized, methods of deriving the solution are presented in Cantó et al. (2000) and Silich et al. (2004). The basic model is completely specified by only three parameters: the energy and mass injection rates ($\dot{E}_{\rm tot}, \dot{M}_{\rm tot}$); and the radius of the starburst region ($R_\star$) within which the energy and mass are injected.

CC present the stationary solution to the hydrodynamical equations as a function of the Mach number $M = v/c_{\rm s}$, where v is the local speed of the flow and the sound speed is $c_{\rm s} = \sqrt{(\gamma P / \rho)}$. The pressure P, density ρ and adiabatic index γ have their normal meanings. At radii $r < R_\star$ mass and energy are injected at a uniform constant rate per unit volume $q_M = \dot{M}_{\rm tot}/V_\star$ and $q_E = \dot{E}_{\rm tot}/V_\star$, where the starburst volume $V_\star = 4\pi R_\star^3/3$, and the solution for the Mach number is

$$\left(\frac{3\gamma + 1/M^2}{1 + 3\gamma} \right)^{-\frac{(3\gamma+1)}{(5\gamma+1)}} \left(\frac{\gamma - 1 + 2/M^2}{1 + \gamma} \right)^{\frac{(\gamma+1)}{2(5\gamma+1)}} = \frac{r}{R_\star}. \quad (1)$$

This approach to the energy and mass injection implicitly assumes that the exact manner in which stars return mechanical energy to the ISM can be ignored due to rapid local thermalization and mixing, i.e. individual stellar winds and SN blast waves collide and merge on spatial scales small compared to the size of the starburst region. If radiative energy losses are to be small then these collisions must occur with a time shorter than the cooling time scale for stellar wind bubbles or supernova remnants (SNRs). Theoretical investigations of some of these issues may be found in Larson (1974), Heckman et al. (1990), Cantó et al. (2000), Melioli & de Gouveia Dal Pino (2004) and Melioli et al. (2005).

At larger radii $r > R_\star$ then $q_M = q_E = 0$, and the solution is

$$M^{\frac{2}{\gamma-1}} \left(\frac{\gamma - 1 + 2/M^2}{1 + \gamma} \right)^{\frac{(\gamma+1)}{2(\gamma-1)}} = \left(\frac{r}{R_\star} \right)^2. \quad (2)$$

For any given fractional radius $r/R_\star$ the Mach number is found using a numerical root-finding technique (in our case the Newton-Raphson method) on the appropriate equation.

To obtain the density at any radius $r < R_\star$ we integrate Equation 1 of CC to obtain

$$\rho = \frac{q_M r}{3 v}. \quad (3)$$

Within the starburst region the gas density, pressure and temperature vary only slowly with radius, with maxima at $r = 0$. The central density is effectively determined by the rate at which the injected material can flow out of the starburst region, $\rho_{\rm c} \propto \dot{M}_{\rm tot}/(4\pi R_\star^2 v_\infty)$ where v_∞ is the terminal velocity of the wind at large radius, and the central temperature is set by the energy injected per particle. More specifically, the central temperature and density are $T_{\rm c} = 0.4 (\mu m_{\rm H} \dot{E}_{\rm tot})/(k \dot{M}_{\rm tot})$ and $\rho_{\rm c} = 0.296 \dot{M}_{\rm tot}^{3/2} \dot{E}_{\rm tot}^{-1/2} R_\star^{-2}$ for $\gamma = 5/3$.

At radii $r \geq R_\star$ the mass flow rate through the spherical surface of radius r is equal to the total mass injection rate within the starburst region, so the density is

$$\rho = \frac{q_M R_\star^3}{3 \nu r^2}. \tag{4}$$

To derive the local velocity of the flow v we must first determine the speed of sound. If we make the assumption that the flow is adiabatic then we can obtain the speed of sound at any point ($r < R_\star$ or $r \geq R_\star$), as we know the Mach number and the initial energy per particle is conserved. Specifically we solve Equation 3 of CC and substitute for ρ using Equation 3, to obtain

$$c_s^2 \left(\frac{M^2}{2} + \frac{1}{\gamma - 1} \right) = \frac{\dot{E}_{tot}}{\dot{M}_{tot}}. \tag{5}$$

The speed of the flow at any point is then simply $v = M c_s$. For $r < R_\star$ the flow is subsonic, with $u \propto r$. The sonic point is reached at $r = R_\star$, beyond which the flow velocity rapidly tends toward the terminal velocity $v_\infty = \sqrt{2} \dot{E}_{tot}^{1/2} \dot{M}_{tot}^{-1/2}$.

With the density ρ and the speed of sound c_s determined at every point within the flow the thermal pressure P is also now known. The kinetic temperature $T = \mu m_H P / \rho k$, where $\mu m_H \approx 1.02 \times 10^{-24} \, \mathrm{g \, cm^{-3}}$ is the mean mass per particle for a fully ionized plasma of Solar composition.

Numerically we derive the gas density, temperature and velocity as a function of radius, iterating outward in thin radial shells. The numerical implementation we use is based on code originally created by Ian Stevens (Stevens & Hartwell 2003). This semi-analytical code reproduces the density and pressure to within 0.1% of the values predicted by the full 2-D hydrodynamical simulation using the VH-1 code for a spherical starburst region. The scaling used to approximate a non-spherical starburst region using the spherical CC model is described in Appendix B.

Figure 3 presents the radial variation in several fluid variables and associated derived quantities for one particular set of input parameters, as predicted using our 1-dimensional CC model code.

3.3. Parameters of the M82 nuclear starburst

3.3.1. The starburst age and magnitude

The flow times for the region of interest ($r \leq 500$ pc) are short (a few Myr) compared to the lifetime of the massive stars powering the flow (~ 30 Myr). The properties of the starburst region will very rapidly approach those of the steady-state CC solution after any change in the energy and mass injection rate.

Nevertheless, in order to apply the CC model to M82 we must determine the history (i.e. age and star formation rate as a function of time) of the starburst event in order to derive the current mechanical energy and mass injection rates and the elemental abundances in the injected gas. Furthermore, determining the degree to which the M82 starburst event can be treated as one the simple limiting cases of either a single instantaneous burst (SIB) or as continuous star formation (CSF) is important, in particular for comparison to Starburst99 models (Leitherer et al. 1999).

Recent observational studies have greatly expanded our knowledge of M82's global star formation history since its close encounter with M81 approximately 0.6 — 1 Gyr ago (see e.g. de Grijs 2001). Nevertheless significant gaps still remain in our understanding of the history of the nuclear starburst.

Exterior to the central kiloparsec star formation appears to have peaked ~ 600 Myr ago in a burst of comparable intensity to the current nuclear starburst event, but star formation effectively ceased in the disk $\sim 20 - 30$ Myr ago (de Grijs et al. 2001; Mayya et al. 2006).

Within the central kiloparsec (projected separations from the nucleus of $r \leq 500$ pc) the majority of recent studies have concentrated on the ~ 200 compact star clusters found there (O'Connell et al. 1995; Melo et al. 2005). The brightest ~ 20 star clusters typically appear to have ages ~ 5 — 10 Myr (Satyapal et al. 1997; McCrady et al. 2003), although two massive clusters (M82-F and M82-L) at the edge of this region have ages of 60 ± 20 Myr (Smith & Gallagher 2001; Smith et al. 2006a). Förster Schreiber et al. (2003a,b) present a detailed analysis of the NIR emission (1 — 45μm) from a variety of regions within $r \leq 250$ pc, and find that two bursts (of ages ~ 5 and ~ 10 Myr respectively) are required in each region to simultaneously explain the strength of both nebular emission features and CO absorption from Red Super Giant (RSG) stars. This work, and the estimated ages of the brightest star clusters, indicates that the nuclear star formation is not well represented as a single instantaneous starburst event.

Note that the cluster-based studies do not provide a complete view of the starburst, as they are mainly observed in regions of lower-than-average extinction[5] toward the nucleus (Smith et al. 2006a). Nor does this work strongly constrain the star formation rate between 10 — 60 Myr ago. Old clusters in this age range, of similar mass to the bright clusters, would be considerably fainter and thus harder to detect than the $t \sim 10$ Myr-old clusters[6], due to the rapid decrease of the ionizing and bolometric output at ages $t \gtrsim 10$ Myr. UV spectroscopic studies of nearby low-obscuration starbursts have shown that the massive star population within the clusters is typically younger the the field massive star population (see e.g. Tremonti et al. 2001; Chandar et al. 2005). The probable cause for this effect is the gradual dissolution of the massive star clusters on times scales of ~ 10 — 30 Myr (for a recent review see de Grijs & Parmentier 2007, and references therein). We are not aware of any similar UV study of the field stellar population in M82's nucleus, so there is no direct evidence for the presence of star formation intermediate in age between the $t \sim 10$ Myr-old clusters and the $t \sim 60$ Myr-old clusters. Nevertheless it remains very plausible that significant star formation continued in between the two periods.

Another reason to suspect that the nuclear burst has been active for longer than ~ 10 Myr is the dynamical age of the Hα cap, a large nebular feature associated with the superwind at a height $z \sim 12$ kpc above the mid-plane of the M82 (Devine & Bally 1999; Lehnert et al. 1999). Its true space velocity is unknown, but assuming a mean velocity of $v_{H\alpha} = 600 \, \mathrm{km \, s^{-1}}$ equivalent to that of the Hα filaments in the lower wind (McKeith et al. 1995; Shopbell & Bland-Hawthorn 1998) it would have taken ~ 20 Myr to reach its current location if its origin was within the disk of the galaxy.

---

[5] The typical measured extinction towards the clusters is $A_V \sim 2$ — 6 magnitudes, see Melo et al. (2005).

[6] Note that this statement, and the previously mentioned cluster ages, is based on single star evolutionary models. Mas-Hesse & Cerviño (1999) argue that if binary systems are taken into account the strongly ionizing phase of a single coeval cluster can last up to ~ 30 Myr after formation, and that the cluster can simultaneously produce nebular emission and have a substantial number of RSGs. If this is indeed the case then the clusters identified as having ages of ~ 10 Myr may be as old as ~ 30 Myr.
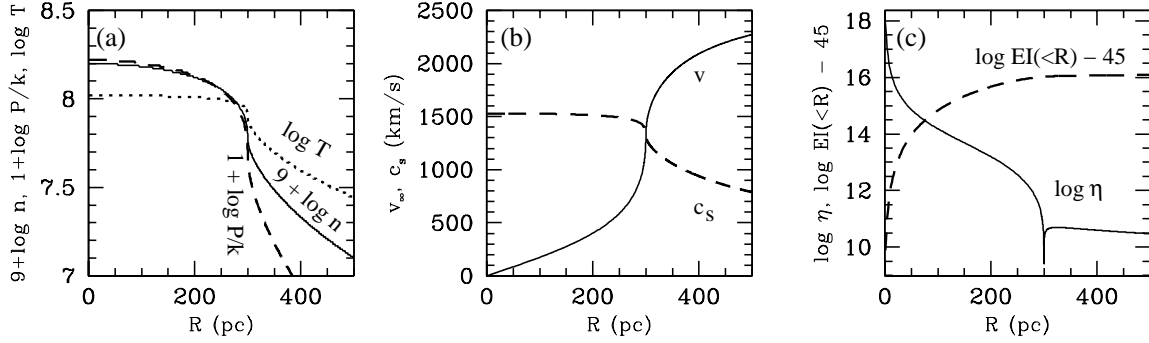
FIG. 3.— (a) An example of the radial CC solution described in § 3.2. Note the relatively uniform number density, thermal pressure and temperature within the assumed starburst region of radius $R_\star = 300$ pc, and rapid drop in those parameters outside the starburst region. The net energy and mass injection rates assumed are $\dot{E}_{\rm tot} = 3.1 \times 10^{42}$ erg s^{-1} and $\dot{M}_{\rm tot} = 1.4\, M_\odot$ yr^{-1}. (b) Local wind velocity v and sound speed $c_{\rm s}$. (c) Logarithms of the ionization-state-related parameter η (Equation 14) and cumulative volume emission integral $EI(<R)$. The plasma is in ionization equilibrium when $\log \eta \geq 12$. Values are given in c.g.s units unless it is stated otherwise.

We thus choose to treat M82's nuclear starburst as having experienced a uniform rate of star formation since the onset of the burst $t_{\rm burst}$ years ago, with negligible star formation before that time. We will treat $t_{\rm burst}$ as a model parameter in the range 10 — 50 Myr.

In Table 4 we present the bolometric luminosity, and total SN plus stellar wind energy and mass injection rates (all per unit star formation rate) for continuous star formation models calculated using version 5.1 of Starburst99 population synthesis code (Leitherer et al. 1999). The star formation rate is $S = 1\, M_\odot$ yr^{-1} for a Salpeter IMF between the mass limits of 1 — $100\, M_\odot$. For a Kroupa (2001) IMF between the mass limits 0.01 — $100\, M_\odot$ producing the same total mass of massive stars (mass range 8 — $100\, M_\odot$) as in the Salpeter IMF model, the star formation rate is a factor 1.76 times larger. The Geneva stellar evolutionary tracks for an initial metallicity equal to Solar, and with high stellar wind mass loss rates, were used.

The total 8 — 1000μm IR luminosity of M82 is $L_{\rm IR} = 5.8 \times 10^{10}\, L_\odot$, based on the latest re-calibrated $12 - 100\mu$m IRAS fluxes (Sanders et al. 2003). IR emission dominates M82's spectral energy distribution, so by equating $L_{\rm IR}$ to the starburst bolometric luminosity for each assumed age yields star formation rates S between 4 — $6\, M_\odot$ yr^{-1} (Salpeter IMF). These values and the associated SN plus stellar wind energy and mass injection rates are tabulated in Table 4. By way of comparison the formulae in Kennicutt (1998), which assume CSF with a large age, give a star formation rate of $S = 3.9\, M_\odot$ yr^{-1} for M82 based on $L_{\rm IR}$, when corrected to the 1 — $100\, M_\odot$ mass range Salpeter IMF we use.

These star formation rates are not unreasonable. Over the time scale of interest the net mass of stars formed is at maximum $\sim 50\%$ of the dynamical mass of $\sim 7 \times 10^8\, M_\odot$ within $r = 250$ pc (Götz et al. 1990), even if we assume a Kroupa IMF extending down to a lower mass limit of $0.01\, M_\odot$.

3.3.2. *The total size of the starburst region*

The brightest region of diffuse non-thermal 5 GHz radio emission in M82 subtends an angular extent of $\sim 43'' \times 6''$ (~ 750 pc $\times 105$ pc), the same region occupied by the compact radio sources presumed to be young SN remnants (Kronberg et al. 1985; Muxlow et al. 1994). This is similar to the size of the region occupied by the brightest star clusters seen in the NIR, $\sim 58'' \times 8''$ (~ 1015 pc $\times 140$ pc, McCrady et al. 2003). These major-axis angular diameters closely match the base of the superwind as measured by the

region of split optical emission lines, which has a diameter of $\sim 50''$ Götz et al. (1990).

If we approximate the starburst region as a flat cylinder of diameter $d_\star$ and total height $h_\star$ then the starburst volume $V_\star = \pi (d_\star/2)^2 h_\star$ and surface area $S_\star = \pi d_\star(h_\star + d_\star/2)$ in each case is $V_{\star,1} = 4.6 \times 10^7$ pc^3, $S_{\star,1} = 1.1 \times 10^6$ pc^2 (5 GHz) and $V_{\star,2} = 1.1 \times 10^8$ pc^3 , $S_{\star,2} = 2.1 \times 10^6$ pc^2 (NIR). The equivalent spherical CC model should then have a starburst region radius of $R_{\star,1} = 300$ pc or $R_{\star,2} = 405$ pc (Appendix B).

The starburst in M82 is possibly concentrated along the stellar bar (see e.g. Achtermann & Lacy 1995; Westmoquette et al. 2007), and hence is more geometrically complex than a uniform disk. Furthermore star formation may not have occurred simultaneously throughout the full starburst region, but evidence for inwardly or outwardly propagating star formation within $r \lesssim 500$ pc of the nucleus remains inconclusive (Förster Schreiber et al. 2003a). Exploring the full significance of these effects requires 3-dimensional hydrodynamical simulations that are outside the scope of this paper.

However we can investigate the significance of concentrating the supernova activity within a smaller disk-like region than the two considered above. We adopt the starburst disk geometry used in Strickland & Stevens (2000) which has $d_\star = 300$ pc and $h_\star = 60$ pc. This produces significantly lower starburst volumes and surface areas: $V_{\star,3} = 4.2 \times 10^6$ pc^3 and $S_{\star,3} = 2.0 \times 10^5$ pc^2. The equivalent spherical starburst radius is $R_{\star,3} = 126$ pc.

For the majority of the models we consider we adopt the first starburst region geometry described above: a disk of diameter $d_\star = 750$ pc and total height $h_\star = 105$ pc (or $R_{\star,1} = 300$ pc for the scaled CC models). The effect of the size of the starburst region is explored using the scaled CC model with radii $R_{\star,2} = 405$ pc and $R_{\star,3} = 126$ pc.

3.3.3. *The effective energy and mass injection rates*

The most significant contributors to the energy and mass return rates in a starburst event are core-collapse SNe and the stellar winds from the massive stars. Stellar winds are thought to contribute an order of magnitude less mechanical energy than the SNe (assuming equal thermalization efficiencies), but they may contribute up to $\sim 50\%$ of the total mass returned to the ISM (Leitherer, Robert, & Drissen 1992; Leitherer & Heckman 1995). As described above, we used the Starburst99 population synthesis code to find the combined SNe plus stellar wind energy and mass injections rates for a continuous burst of star formation as a function of age.

TABLE 4
CONTINUOUS STAR FORMATION MODELS FOR M82.

Age (Myr) (1)	$L_{\rm bol}/\mathcal{S}$ ($L_\odot\,M_\odot^{-1}$ yr) (2)	$\dot{E}_{\rm SN+SW}/\mathcal{S}$ (erg s$^{-1}\,M_\odot^{-1}$ yr) (3)	$\dot{M}_{\rm SN+SW}/\mathcal{S}$ ($\cdots$) (4)	$\mathcal{S}$ ($M_\odot$ yr^{-1}) (5)	$\dot{E}_{\rm SN+SW}$ (erg s^{-1}) (6)	$\dot{M}_{\rm SN+SW}$ ($M_\odot$ yr^{-1}) (7)
10	9.6×10^9	3.1×10^{41}	0.19	6.1	1.9×10^{42}	1.1
20	1.1×10^{10}	5.1×10^{41}	0.26	5.1	2.6×10^{42}	1.3
30	1.2×10^{10}	6.5×10^{41}	0.29	4.7	3.1×10^{42}	1.4
40	1.3×10^{10}	7.1×10^{41}	0.31	4.5	3.2×10^{42}	1.4
50	1.3×10^{10}	6.9×10^{41}	0.31	4.4	3.0×10^{42}	1.3

NOTE. — Column 1: Age since the onset of continuous star formation. Column 2: Starburst radiated bolometric luminosity per unit star formation rate. Column 3: Mechanical energy injection rate due to SNe and stellar winds per unit star formation rate. Column 4: Mass injection rate due to SNe and stellar winds per unit star formation rate. Note that the values in Columns 2 – 4 are specific to a Salpeter IMF between the lower and upper mass limits of $1 - 100\,M_\odot$. Column 5: Star formation rate $\mathcal{S}$ derived from $L_{\rm IR}/(L_{\rm bol}/\mathcal{S})$, where $L_{\rm IR}$ is the observed IR luminosity of M82. Column 6: The mechanical energy injection rate associated with this SFR. Column 7: The mass injection rate associated with this SFR. See § 3.3.1 for details on the stellar evolutionary tracks and stellar wind models used.

Note that the values of $\dot{E}_{\rm SN+SW}$ and $\dot{M}_{\rm SN+SW}$ given in Table 4 have not been corrected for any initial mechanical energy losses due to radiation before thermalization occurs (the thermalization efficiency ϵ) or for mass loading by the addition of cold ambient ISM (with a rate $\dot{M}_{\rm cold}$).

The thermalization efficiency and degree of mass loading are expected to be a function of the local gaseous environment the massive stars find themselves in, as well as the local supernova rate per unit volume and the density of massive stars. Low ambient gas density and/or high SN rate per unit volume should lead to a higher hot gas filling factor, which in turns increases the thermalization efficiency by reducing the initial radiative energy losses (Heckman et al. 1990). However, at very high stellar densities the SN and stellar wind ejecta may itself become dense enough to cause drastic energy losses, e.g. within the central regions of super star clusters (Silich et al. 2004; Tenorio-Tagle et al. 2007).

To account for these factors we assume that only a fraction ζ of all the SNe and stellar winds occur in regions where conditions lead to non-negligible thermalization, and the mean thermalization efficiency in these regions is what we define as ϵ. Essentially ζ is a modification to the total star formation rate of the starburst to account for localized spatial variations within the starburst of the SN and stellar wind feedback. We will refer to ζ as the participation fraction, as it is effectively the fraction of the total star formation that is actually involved in driving the superwind. For the remaining fraction 1-ζ of the SNe and stellar winds we assume that radiative energy losses are so significant that no mechanical energy is supplied to the starburst region, and that the ejecta never becomes part of the outflow. We treat ζ as a model variable, and refer the reader to Appendix C for a discussion of plausible values for ζ given the gas content of the starburst and the star cluster mass function.

The net energy injection rate into the hot volume-filling gas in the starburst region is

$$\dot{E}_{\rm tot} = \epsilon\zeta\dot{E}_{\rm SN+SW}. \tag{6}$$

The net mass injection rate is

$$\dot{M}_{\rm tot} = \zeta\dot{M}_{\rm SN+SW} + \dot{M}_{\rm cold} = \beta\zeta\dot{M}_{\rm SN+SW}, \tag{7}$$

where the mass loading factor β is a parameter commonly used to indicate the relative amount of mass loading. If $\beta = 1$ then the wind is not mass loaded. In this paper we consider only mass loading that operates within the starburst re-

gion, i.e. central mass loading in the terminology adopted by Suchkov et al. (1996) and Strickland & Stevens (2000).

Written as a function of the thermalization efficiency, the mass loading factor and participation factor, the central temperature, pressure and density are

$$T_{\rm c} = 0.4\,\frac{\mu m_{\rm H}\,\epsilon\,\dot{E}_{\rm SN+SW}}{k\,\beta\,\dot{M}_{\rm SN+SW}}, \tag{8}$$

$$P_{\rm c} = 0.118\,\frac{\epsilon^{1/2}\,\beta^{1/2}\,\zeta\,\dot{E}_{\rm SN+SW}^{1/2}\,\dot{M}_{\rm SN+SW}^{1/2}}{R_\star^2}, \tag{9}$$

and

$$\rho_{\rm c} = 0.296\,\frac{\zeta\,\beta^{3/2}\,\dot{M}_{\rm SN+SW}^{3/2}}{\epsilon^{1/2}\,\dot{E}_{\rm SN+SW}^{1/2}\,R_\star^2}. \tag{10}$$

The central temperature is thus linearly proportional to the ratio of the mechanical energy thermalization efficiency to the mass loading factor, and independent of the size of the starburst region $R_\star$ or participation factor ζ. Thus it is an excellent diagnostic tool for quantifying the effects of feedback, provided that this temperature can be accurately measured.

The terminal velocity of the wind fluid

$$v_\infty = \left(\frac{2\,\epsilon\,\dot{E}_{\rm SN+SW}}{\beta\dot{M}_{\rm SN+SW}}\right)^{1/2} \equiv \left(\frac{5kT_{\rm c}}{\mu m_{\rm H}}\right)^{1/2} \tag{11}$$

is also a function of ϵ/β. An observational determination of v_∞ is beyond the capabilities of current X-ray observatories, but the X-ray Microcalorimeter Spectrometer (XMS) instrument on the future International X-ray Observatory (IXO) will provide the high resolution non-dispersive X-ray spectroscopy necessary to directly measure the velocity of the hot phases in superwinds.

3.3.4. *The metal abundance within the wind fluid*

The mixed SN ejecta and stellar wind material will be enriched in heavy elements compared to the cooler ambient ISM within the starburst region. As the emissivity of the thermal X-ray emission from a hot plasma depends strongly on the metal abundance of the hot plasma it is necessary to consider both SN-related enrichment and dilution via mass loading.

If we assume mass-loading is associated with efficient mixing, then the elemental abundance $Z_{i,\rm WF}$ of an element i in the

wind fluid is

$$Z_{i,\text{WF}} = \frac{Z_{i,\text{SN+SW}}\zeta\dot{M}_{\text{SN+SW}} + Z_{i,\text{cold}}\dot{M}_{\text{cold}}}{\zeta\dot{M}_{i,\text{SN+SW}} + \dot{M}_{\text{cold}}} = \frac{Z_{i,\text{SN+SW}} + (\beta-1)Z_{i,\text{cold}}}{\beta}$$

(12)

where $Z_{i,\text{SN+SW}}$ is the abundance of the element in the SN plus stellar wind ejecta and $Z_{i,\text{cold}}$ is the abundance in the ambient ISM, and we have made use of Equation 7 which defines β.

The primary elemental coolants for plasmas with temperature $T \gtrsim 10^5$ K are oxygen, neon and iron (e.g. see Sutherland & Dopita 1993). Iron is of particular importance for this work given the $E \sim 6.7$ keV and $E \sim 6.9$ keV lines from helium-like and hydrogen-like iron ions. Elements such as S, Ar and Ca also produce weaker X-ray lines at energies $E > 2$ keV that may also serve as a diagnostic of the wind-fluid.

Limongi & Chieffi (2007) present the IMF-averaged SN ejecta (both SN II and SN Ib/c) element abundances with respect to Solar[7]. Their stellar evolution models include mass loss due to stellar winds, but the quoted yields do not include the hydrogen and lighter elements returned to the ISM by the winds. They find $Z_{\text{Fe,SN}} \sim 7Z_{Fe,\odot}$, $Z_{\text{O,SN}} \sim 6Z_{O,\odot}$, $Z_{\text{Ne,SN}} \sim 10Z_{Ne,\odot}$, $Z_{\text{S,SN}} \sim 5Z_{S,\odot}$, $Z_{\text{Ar,SN}} \sim 4Z_{Ar,\odot}$ and $Z_{\text{Ca,SN}} \sim 3Z_{Ca,\odot}$. Note the low O/Fe abundance ratio compared to the IMF-averaged yields presented in Gibson et al. (1997), which is most probably a consequence of wind mass loss in the stellar evolution models used by Limongi & Chieffi (2007).

The time-averaged nature of an IMF-averaged yield is appropriate for continuous star formation with an age of $t \gtrsim 20$ Myr, but the abundances in the ejecta for a younger or instantaneous burst may differ from that in Limongi & Chieffi (2007). To investigate this, and the effect of using a different set of SN yields, we computed the abundances of the combined SN ejecta and stellar wind material from the yields given by Starburst99. Starburst99 includes wind yields by combining the stellar evolutionary wind mass loss rates with observed stellar surface abundances. SN yields are based on Woosley & Weaver (1995) for SN type II, but note that the the stellar evolution models that Woosley & Weaver used did not in general include wind mass loss. Starburst99 also assumes that stars that become Wolf-Rayet stars (initial mass $M_\star \gtrsim 33 M_\odot$) are assumed to explode as SN type Ib/c and contribute no metals to the final yields. For a continuous star formation model the SN plus stellar wind ejecta abundances predicted by Starburst99 are relative constant for ages $t \geq 15$ Myr after the onset of the burst, at levels of $Z_{\text{Fe,SN+SW}} \sim 4Z_{Fe,\odot}$, $Z_{\text{O,SN+SW}} \sim 6Z_{O,\odot}$, and $Z_{\text{S,SN+SW}} \sim 14Z_{S,\odot}$ (Starburst99 does not calculate the yields of Ne, Ar and Ca).

Given the uncertainties we will adopt $Z_{\text{Fe,SN+SW}} = 5Z_{Fe,\odot}$ for these models. For computational convenience we will further assume the same abundance relative to Solar for the other elements.

The stellar and H II region O and Ne abundances in M82 are Solar or higher (Achtermann & Lacy 1995; Origlia et al. 2004; Smith et al. 2006b). The are very few measurements of iron abundances, the only one we are aware of is that of Origlia et al. (2004) who derive a stellar iron abundance of $Z_{\text{Fe}} = 0.46^{+0.26}_{-0.17}Z_{\text{Fe},\odot}$ from NIR spectroscopy. The total baryonic mass of M82 is $\sim 2 \times 10^{10} M_\odot$ based on its peak rotational velocity (see Strickland et al. 2004a). Galaxies of this mass have a mean nebular oxygen abundance of $\sim 1.2Z_{O,\odot}$

---

[7] All abundances quoted in this paper are relative to the scale defined in Anders & Grevesse (1989).

(on the Anders & Grevesse 1989 scale), based on the galaxy mass-metallicity relationship (Tremonti et al. 2004). Thus the measured metallicity of the stellar population and the warm ISM in M82 are not unusual given its mass, nor do they suggest that the ambient ISM has been significantly enriched with nucleosynthetic products from the current starburst. We adopt $Z_{\text{Fe,cold}} = 1Z_{\text{Fe},\odot}$ for our models, again assuming the same value for all other elements.

3.4. *Broad-band cooling and X-ray line emission*

The luminosity per unit volume $\mathcal{L}$ (erg s^{-1} cm^{-3}) due to the thermal emission from an element of gas of density ρ, temperature T and metal abundance Z is

$$\mathcal{L} = n_e n_{\text{H}}\Lambda(T,Z) = \frac{\chi_{\text{H}}(1+\chi_{\text{H}})}{2m_{\text{H}}^2}\rho^2\Lambda(T,Z),$$

(13)

where $\chi_{\text{H}} \approx 0.71$ is the mass fraction of hydrogen for a Solar abundance plasma, m_{H} is the mass of a hydrogen atom and $\Lambda(T,Z)$ is the cooling function for the specific energy band or line transition being considered.

For broad-band X-ray emission, or the total cooling rate, the cooling function for a hot optically thin plasma may be split into a metallicity-independent component $\Lambda_{\text{H+He}}(T)$ and metallicity-dependent component $\Lambda_Z(T)$ (evaluated for Solar abundance), such that $\Lambda(T,Z) = \Lambda_{\text{H+He}}(T) + Z \times \Lambda_Z(T)$, where Z is the metal abundance with respect to the Solar. This assumes that the relative metal abundances are Solar, as otherwise the contribution from each element must be considered separately.

To assess the total cooling rate we use the zero-field non-equilibrium cooling functions from Sutherland & Dopita (1993). We calculated the metallicity-dependent cooling Λ_Z from their published Solar and zero metallicity cooling functions. At temperatures above $T \sim 5 \times 10^6$ K (typical of the vast majority of the models we will consider) the difference between equilibrium and non-equilibrium cooling functions is negligible.

To calculate the cooling functions for the $E = 2 - 8$ keV hard X-ray band and the Heα and Lyα like lines of S, Ar, Ca and Fe we used version 1.3.1 of APEC hot plasma code (which assumes collision ionization equilibrium), accessed using the XSPEC spectral fitting program (Arnaud 1996; Smith et al. 2001). For the line emission from any specific element i the cooling function is an exactly linear function of the metallicity Z_i, i.e. $\Lambda(T,Z_i) = Z_i \times \Lambda_Z(T)$.

In Fig. 4 we plot the total and $2 - 8$ keV cooling functions (split into their metallicity-independent and metallicity-dependent components) that we use in our calculations. The line-specific cooling functions for hydrogen-like and helium-like sulphur, argon, calcium and iron for unit metal abundance are also shown.

The X-ray line emissivities we use apply to hot gas in collisional ionization equilibrium (CIE). In our the calculations using the scaled CC model we evaluate the following expression in each radial shell as we numerically integrate outwards:

$$\eta = \frac{n_e}{v\left|\frac{d\log T}{dr}\right|}$$

(14)

If the ionization parameter $\eta \gtrsim 10^{12}$cm^{-3}s then the plasma is likely to be in CIE (Masai et al. 2002). If $\eta < 10^{12}$ cm^{-3} s then the outflowing gas is over-ionized and in recombining non-equilibrium. Masai et al. show that the broad band X-ray emissivity of such a recombining plasma is less than that of a
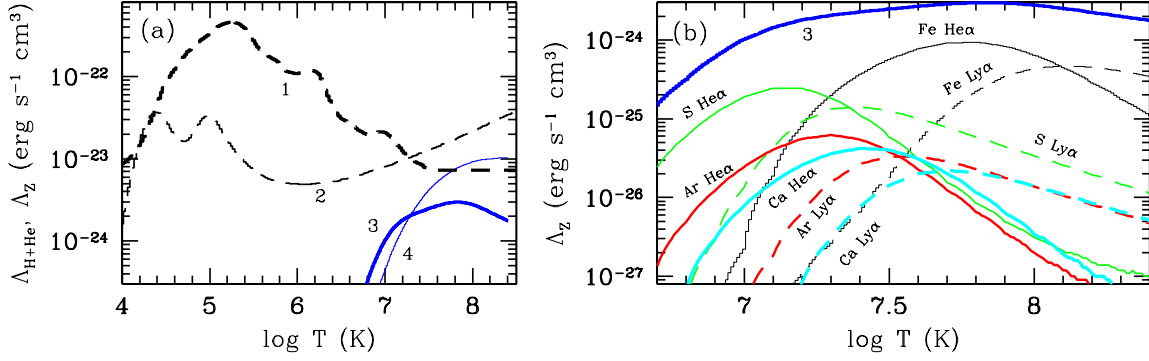
FIG. 4.— (a) The broad band cooling functions used in the model calculations. The total cooling due to metals for unit metal abundance with respect to Solar abundance (1) and cooling from hydrogen and helium only (2) for non-equilibrium cooling are both from Sutherland & Dopita (1993). The APEC plasma code (Smith et al. 2001) was used to calculate the emission in the hard X-ray energy band ($E = 2 - 8$ keV) from metals (3) and hydrogen plus helium (4), assuming collisional ionization equilibrium. (b) X-ray cooling curves per unit metal abundance for helium-like and hydrogen-like ions of S, Ar, Ca and Fe in comparison to the 2–8 keV cooling curve for all metals (3).

CIE plasma. The ionization parameter η scales with thermalization efficiency and mass loading proportionally as β^2/ϵ, as increasing the mass loading or decreasing the thermalization efficiency acts both to increase the plasma density and decrease the outflow velocity.

For parameters appropriate to M82 we find that the plasma is typically in CIE at radii $r \lesssim R_\star$ even when $\epsilon = \beta = 1$. Even if we integrate the emission out to radii $\gg R_\star$ the total luminosity is dominated by emission from within $R_\star$, justifying our use of CIE emissivities. The radial variation in η and the cumulative emission integral $EI(< R)$ shown in Fig 3c demonstrate this for one set of possible model parameters. This result is consistent with the alternative ionization equilibrium and Coulomb relaxation timescale calculations presented in Paper I, which also indicated that the hot plasma within the starburst region should be in ionization equilibrium.

For a single temperature plasma the luminosity is the product of the emission integral EI with the cooling function Λ. The cumulative volume emission integral is defined as $EI(< R) = \int_0^R 4\pi n_e n_H R^2 dR$. For a CC-style radial wind this is dominated by material within the relatively dense starburst region, as shown in Fig 3c. Thus the total emission integral is proportional to

$$EI \propto \rho^2 V_\star \propto \frac{\zeta^2 \beta^3}{\epsilon R_\star} \frac{\dot{M}_{SN+SW}^3}{\dot{E}_{SN+SW}}, \qquad (15)$$

which again increases as either the mass loading factor β is increased, or as the thermalization efficiency ϵ is decreased. However such variations in β and/or ϵ are also associated with a decrease in the central temperature, and for increased mass loading a decrease in the mean metal abundance, so that the net luminosity can ultimately decrease even as increasing β or decreasing ϵ monotonically increase the net emission integral.

3.5. Observational constraints

The primary aim of this project is to assess the range of starburst properties that are consistent with the hard X-ray Fe line-emitting plasma in M82, and which models are deemed acceptable depends on which constraints are used — this is unavoidable. These are not an arbitrary set of observational and conceptual constraints but have been chosen based on realistic physical expectations.

Based on the results and discussion presented in § 2 we adopt the following as the full observational constraints on the properties of the wind fluid within a radius of 500 pc of the center of M82.

- The total X-ray luminosity of the wind fluid in the $E = 2 - 8$ keV energy band must be less than or equal to the broad band luminosity estimated from the ACIS-S observation for the diffuse hard X-ray emission (Table 1), i.e. $\log L_{2-8keV} \leq 39.65$.

- The Fe Heα line luminosity must be consistent with the observed value given in Table 1. In order to be conservative in our estimation of the constraints the observations place on the thermalization efficiency and mass loading, i.e. to accept the largest number of models matching the observational constraints, we adopt the *weakest* constraints on the allowed value of $L_{FeHe\alpha}$, i.e. using the ACIS-S observation rather than the better constrained values from the *ACIS-I* or *XMM-Newton* data sets. Models producing Fe line luminosities within 68.3% confidence region from the ACIS-S observation, $37.96 \leq \log L_{FeHe\alpha} \leq 38.39$, will be judged as matching the constraint on the $E \sim 6.7$ keV line emission. This measurement of $L_{FeHe\alpha}$ is slightly larger than, but still consistent with the line luminosity estimated from the ACIS-I and XMM-Newton observations.

- The Fe Lyα luminosity must be less than or equal to the observationally-determined upper limits, of which the best determined value is from the *XMM-Newton* observation. We specify that $L_{FeLy\alpha}/L_{FeHe\alpha}$ should be ≤ 0.34 for a model to be judged to be consistent with the observational constraints (Table 1).

- The luminosity of the predicted Heα and Lyα-like lines of S, Ar and Ca must be less than or equal to the observed values and/or 99% upper limits. Here the best observational constraints are from the *XMM-Newton* data (Table 3). Acceptable models must then satisfy all of the following: $\log L_{SHe\alpha} \leq 38.19$, $\log L_{SLy\alpha} \leq 37.43$, $\log L_{ArHe\alpha} \leq 37.53$, $\log L_{ArLy\alpha} \leq 37.26$, $\log L_{CaHe\alpha} \leq 37.27$, and $\log L_{CaLy\alpha} \leq 37.14$. Upper limits are used as the S, Ar and Ca-line-emitting plasma is not necessarily the same phase as the Fe-line-emitting plasma.

Models that (a) have total radiative losses less than 30% of the net energy injection rates (see Appendix A) and (b) predict X-ray luminosities consistent with the full set of constraints given above are considered as having successfully matching the full set of constraints.

We will consider the effect of using a different set of observational constraints. These alternatives deliberately ignore what we know about the iron line emission (the iron lines are not used as constraints) and instead attempt to fully account for all of either the broad-band hard X-ray luminosity or the detected S, Ca and Ar line luminosities:

- The total X-ray luminosity of the wind fluid in the $E = 2 - 8$ keV energy band must be within the 3σ envelope given in Table 1 for the model to considered successful, i.e. $39.59 \leq \log L_{2-8keV} \leq 39.71$. In addition the the total radiative losses must be less than 30% of the net energy injection rate. We shall refer to these constraints as the broad-band-only constraints.

- The predicted line luminosities for the S Heα, S Lyα, Ar Heα and Ca Heα must be within $\pm 3\sigma$ of the values given in Table 3 for the best fit to the *XMM-Newton* spectrum. The allowed limits on the Ar Lyα and Ca Lyα line luminosities are the same as given for the full set of constraints. In addition the model must predict broad band and total radiative energy losses less than the upper limits also used in the full set of constraints: $\log L_{2-8keV} \leq 39.65$ and total radiative losses less than 30% of the net energy injection rate. We shall refer to these constraints as the SArCa constraints.

We allow larger ranges in the broad-band or line luminosity ($\pm 3\sigma$) as we found that in practice that it is relatively hard to find regions of parameter space where models can satisfy the broad-band-only or SArCa constraints.

4. SIMULATIONS AND THE RESULTS THEREOF

4.1. *Acceptable values of ϵ and β.*

Mass loading factors of $\beta \sim 10$ or thermalization efficiencies of $\epsilon \sim 0.1$ mark the practical upper and lower limits on these parameters for a M82-like starburst. Each of these values on its own will reduce the central temperature to $T_c \sim 10^7$ K, a temperature at or below which the emissivity of the Fe Heα emission drops dramatically (Fig. 4).

To explore this region of the mass loading and thermalization efficiency parameter space we adopt the following values for the other important model parameters: $\zeta = 1$, a disk-like starburst with $d_\star = 750$ pc and $h_\star = 105$ pc ($R_\star = 300$ pc), $Z_{SN+SW} = 5 Z_\odot$ and $Z_{cold} = 1 Z_\odot$. We treat the starburst as continuous star formation at a rate of $\mathcal{S} = 4.7 M_\odot$ yr^{-1} beginning 30 Myr ago, which leads to $\dot{E}_{SN+SW} = 3.1 \times 10^{42}$ erg s^{-1} and $\dot{M}_{SN+SW} = 1.4 M_\odot$ yr^{-1}. We shall refer to this combination of input model parameters as parameter set A (see Table 5).

We initially computed models covering the full range of $\epsilon : \beta$ parameter space. To prevent the total number of simulations from becoming excessive we considered only a limited number of distinct values for ϵ and β, specifically $\epsilon = 2^{-N}$ and $\beta = 2^N$, where N ranges from 0 to 3 in increments of 0.25, resulting in the computation of 169 models using the 2-dimensional hydrodynamical code described in § 3.1.

We find that only limited regions of parameter space yield models that satisfy any one of the sets of observational constraints we chose to apply (Fig. 5). Furthermore, the regions in $\epsilon:\beta$ parameter space satisfying the different sets of constraints are well separated from one another.

Models that satisfy the full set of observational constraints (labeled F in Fig. 5) have moderately high thermalization efficiencies ($\log \epsilon \gtrsim -0.3$) and moderately low but non-negligible

mass loading ($0.15 \lesssim \log \beta \lesssim 0.3$). These models reproduce the observed Fe line fluxes and limits without overproducing S, Ar or Ca line emission, but in doing so they can only account for a small fraction ($\sim 10 - 25\%$) of the total observed diffuse luminosity of $\log L_{2-8keV} \sim 39.6$ in the $E = 2 - 8$ keV energy band (Fig. 5b).

The range of central thermal pressures found in these matching models, $P_c/k = (1.4 - 2.5) \times 10^7$ K cm^{-3} (given in Table 6) is consistent with estimates of the pressure within the starburst region obtained from optical spectroscopy: $P/k \sim (0.5 - 3) \times 10^7$ K cm^{-3} (Heckman et al. 1990; Smith et al. 2006b; Westmoquette et al. 2007).

To match the observed S, Ar and Ca line fluxes using a wind model (the region labeled SArCa), models require a lower thermalization efficiency and a comparable or slightly higher mass loading factor ($-0.7 \lesssim \epsilon \lesssim -0.4$, $\log \beta \sim 0.4$).

To reproduce the observed diffuse X-ray luminosity in the $E = 2 - 8$ keV energy band with thermal emission alone requires both high thermalization efficiency and high mass-loading factors: $\log \epsilon \gtrsim -0.3$ and $\beta \gtrsim 5$ (the region labeled BB in Fig. 5). Models in this region of parameter space fail to match the full set of observational constraints because they typically predict more S, Ar or Ca emission (the S Lyα luminosity is shown in Fig. 5c) than is observed when the Fe line luminosity is correctly reproduced, or too little Fe Heα emission when they predict less than or equal to the amount of S, Ar or Ca line emission observed.

Thus we can only account for $\lesssim 50\%$ of the observed $E = 2 - 8$ keV diffuse X-ray luminosity with $R = 500$ pc with the sum of the predicted thermal emission from the starburst region and the Inverse Compton X-ray emission (Paper I). We conclude that either our estimate of the Inverse Compton luminosity is in error, or there must be an additional non-thermal or quasi-thermal source of hard X-ray continuum emission within the starburst region (e.g. Dogiel et al. 2002; Masai et al. 2002). Solving this enigma will require higher resolution spectroscopy to establish the shape of the continuum and the ionization state of the line emission.

Models where the total radiative losses are higher than 30% of the energy injection rate, and the adiabatic assumption is no longer valid, are labeled NA in Fig. 5. Note that for these models the temperatures and X-ray luminosities we predict are not valid. The location of this region in $\epsilon : \beta$ space in consistent with the discussion in Appendix A. For M82's star formation rate and starburst region size we find that as long as $\zeta \beta^3/\epsilon^2 \lesssim 1000$ then the adiabatic assumption is applicable to either a disk-like or spherical starburst.

Parameters that give rise to highly radiative winds can be rejected even though we can not predict their exact X-ray luminosities. Cooling is so efficient under such conditions that the central temperature $T_c \ll 10^7$ K and there is no possibility of Fe Heα emission (e.g. Tenorio-Tagle et al. 2007).

To further refine our knowledge of the exact region of the allowed $\epsilon : \beta$ parameter space for M82's starburst we ran a further set of full hydrodynamical simulations a subset of the full $\epsilon : \beta$ grid described above. We used a linearly-spaced grid, varying ϵ between 0.1 and 1.0 in steps of $\Delta \epsilon = 0.05$ and β between 1.0 and 3.0 in steps of $\Delta \beta = 0.1$ (a total of of 494 models).

The predicted regions of allowed parameter space for parameter set A are shown in Fig. 6. This figure also demonstrates that the exact shape of the allowed region using the full set of constraints is most-strongly influenced by the combina-
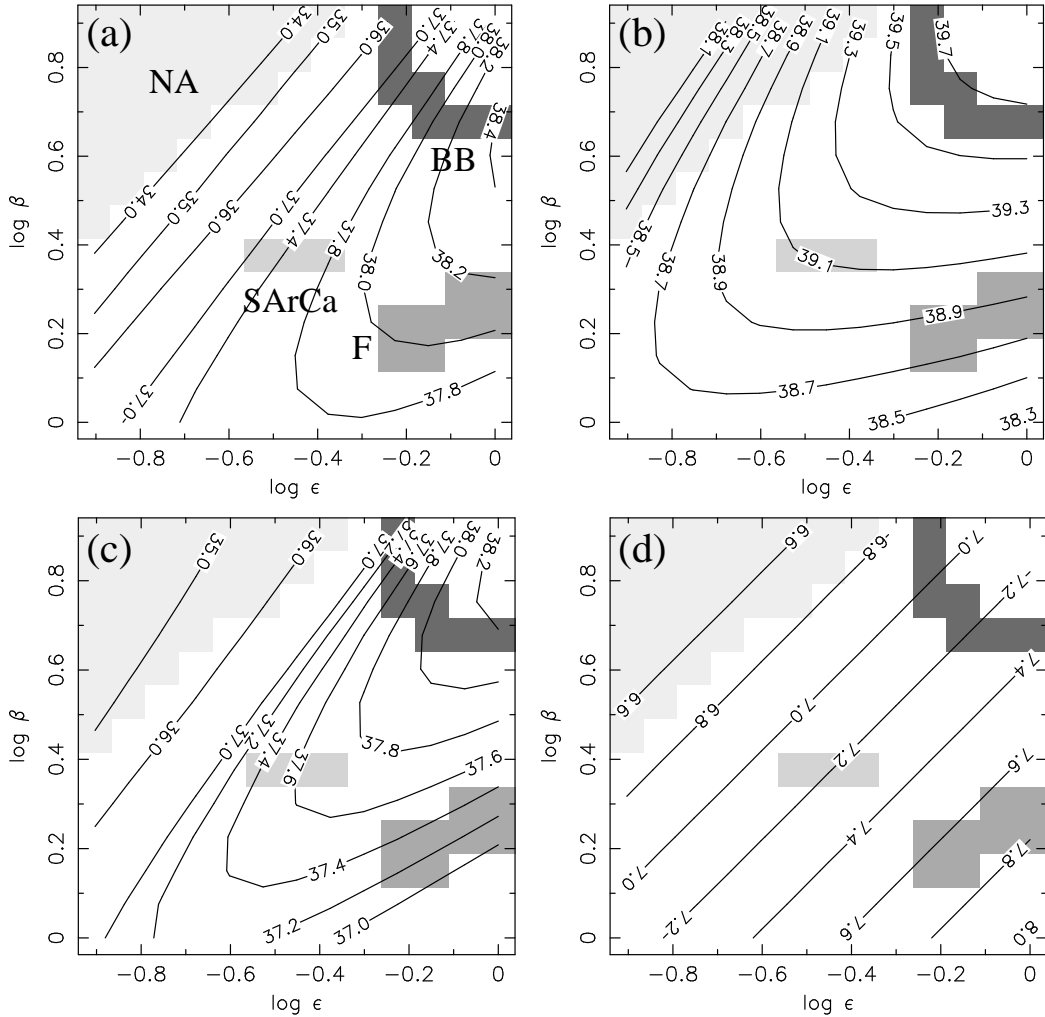
FIG. 5.— Predicted luminosities and temperatures as a function of the input thermalization efficiency ϵ and mass loading factor β, as predicted using the 2-dimensional hydrodynamical simulations with parameter set A (see § 4.1). (a) The logarithm of the Fe Heα luminosity. The grey-shaded region labeled F shows the region of parameter space that matches the full set of observational constraints discussed in § 3.5. The region labeled BB denotes the region satisfying the broadband-only constraints, while the region labeled SArCa satisfies the S, Ar, and Ca line constraints. The region labeled NA denotes the region of parameter space where the adiabatic assumption ceases to the valid. (b) As (a), except the labeled contours show the logarithm of the luminosity in the $E = 2 - 8$ keV energy band. (c) As (a), except the labeled contours show the logarithm of the S Lyα line luminosity. (d) As (a), except the contours show the logarithm of the central plasma temperature T_c in Kelvin.

tion of the constraints on the Fe Heα line and the upper limit on the S Lyα line[8]. For a given value of the thermalization efficiency ϵ the lower boundary of acceptable mass loading factors β is set by requirement to achieve sufficient Fe Heα emission (the necessary condition is $37.96 \leq \log L_{FeHe\alpha} \leq 38.39$), while the maximum β is set by the requirement not to exceed the observed S Lyα luminosity ($\log L_{SLy\alpha} \leq 37.43$).

For a given value of ϵ the highest allowed β is a less likely solution than a lower allowed value of β. The highest allowed values of β produce the entire observed S Lyα flux in the wind fluid, without leaving leeway for S Lyα emission from the soft X-ray-emitting plasma within the starburst region.

Were we to change the S Lyα constraint from an upper limit to a specific range in values around the observed line luminosity the resulting allowed region would be a narrow strip along what is currently the upper β margin of the full allowed region. Adopting such a constraint would be somewhat ad-hoc, given that the S Heα and Ar Heα lines are equally well de-

[8] For this reason we have not provided plots of the S Heα, Ar or Ca line luminosities as a function of ϵ and β.

tected as the S Lyα line (Table 3). Furthermore, an attempt to match the S Heα, Ly α and Ar Heα line fluxes, rather than treating them as upper limits, simultaneously with the Fe Heα line flux leads to no acceptable models being found. Ultimately this is because the S, Ar and Ca line fluxes and upper limits are indicative of a plasma temperature $\log T \lesssim 7.2$ (see Table 2 or the SArCa region on Fig. 6d), yet such a low temperature plasma produces too little Fe Heα emission to match the observations.

As shown in Fig. 7, these same general regions of acceptable parameter space are reproduced in simulations making use of the scaled CC model, although in detail there are minor difference caused by the $\lesssim 30\%$ errors in the luminosity predicted by the scaled CC model compared to the multidimensional hydrodynamical simulations (Appendix B).

4.2. *Other input model parameters.*

Given the computational cost of the full hydrodynamical simulations it is preferable to use the scaled CC model to explore the effect of varying other model parameters such as starburst region size, metal abundance and participation fac-

TABLE 5
COMBINATIONS OF STARBURST MODEL PARAMETERS EXPLORED IN THE
SIMULATIONS.

Parameter Set ... (1)	SF Mode/Age ... (2)	$\dot{E}_{\rm SN+SW}$ (erg s^{-1}) (3)	$\dot{M}_{\rm SN+SW}$ ($M_\odot$ yr^{-1}) (4)	$R_\star$ (pc) (5)	$Z_{\rm SN+SW}$ ($Z_\odot$) (6)	ζ ... (7)
A	CSF / 30 Myr	3.1×10^{42}	1.4	300.0	5.0	1.00
B	CSF / 10 Myr	1.9×10^{42}	1.1	300.0	5.0	1.00
C	SIB / 10 Myr	4.5×10^{42}	2.2	300.0	5.0	1.00
D	CSF / 30 Myr	3.1×10^{42}	1.4	125.5	5.0	1.00
E	CSF / 30 Myr	3.1×10^{42}	1.4	404.9	5.0	1.00
F	CSF / 30 Myr	3.1×10^{42}	1.4	300.0	2.5	1.00
G	CSF / 30 Myr	3.1×10^{42}	1.4	300.0	7.5	1.00
H	CSF / 30 Myr	3.1×10^{42}	1.4	300.0	5.0	0.71
I	CSF / 30 Myr	3.1×10^{42}	1.4	300.0	5.0	0.50

NOTE. — Column 1: Adopted name of combinations of model parameters. Column 2: The mode of star formation assumed, either continuous star formation (CSF) or an single instantaneous burst (SIB) beginning or occurring the specified time before the present. Columns 3 and 4: The mechanical energy and mass injection rates (See § 3.3.1) associated with the assumed star burst. Column 5: The effective starburst radius adopted in calculations using scaled CC model. Column 6: The assumed metal abundance of heavy elements relative to Solar (see § 3.3.4). Column 7: The assumed participation fraction (see § 3.3.3 or Appendix C).
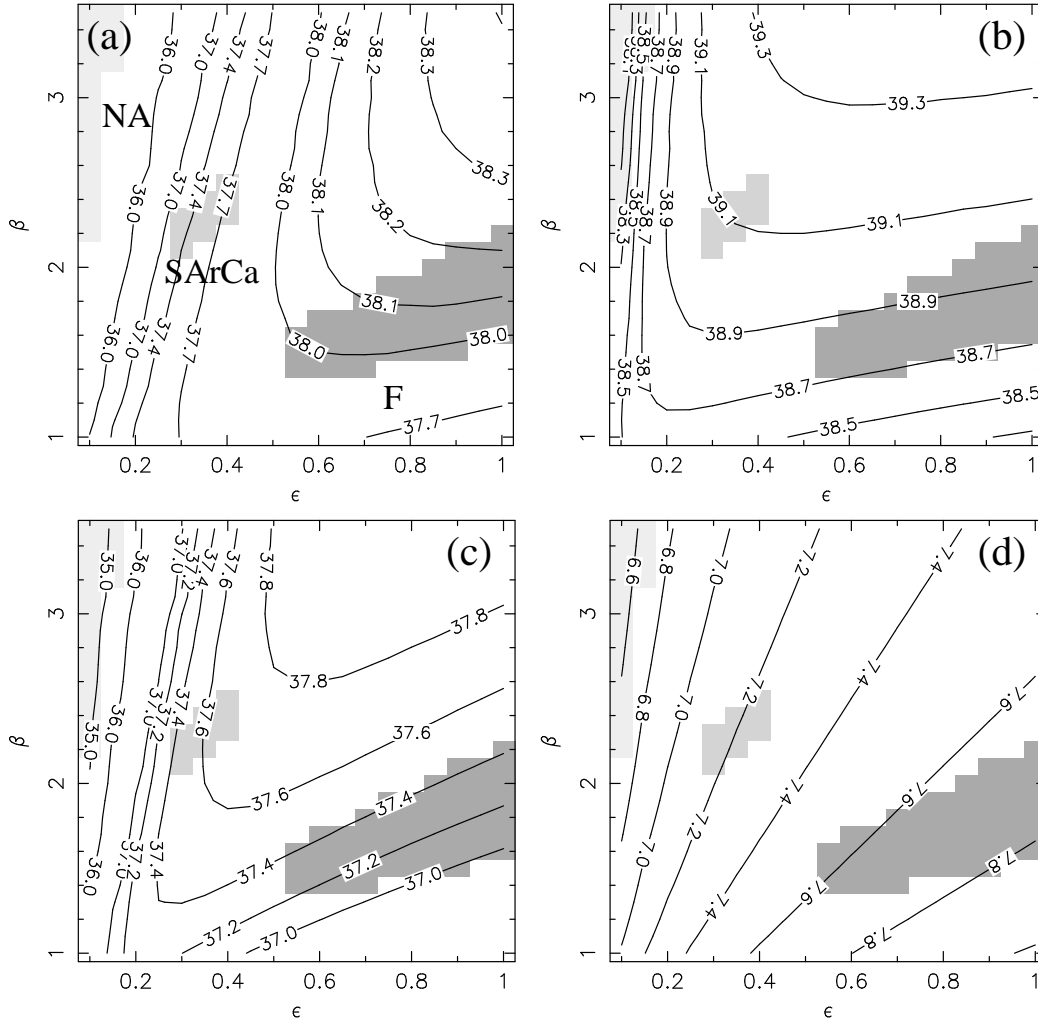

FIG. 6.— As Fig. 5, except using a finer grid of models distributed linearly in a smaller region of $\epsilon : \beta$ parameter space. The numbered contour levels are of log $L_{\rm FeHe\alpha}$ (a), log $L_{\rm 2-8keV}$ (b), log $L_{\rm SLy\alpha}$ (c) and log T_c (d).

tor. Our experience with parameter set A indicates that the scaled CC model reproduces the allowed values of ϵ and β to an accuracy of $\lesssim 0.1$ for the full set of observational constraints that include the Fe lines.
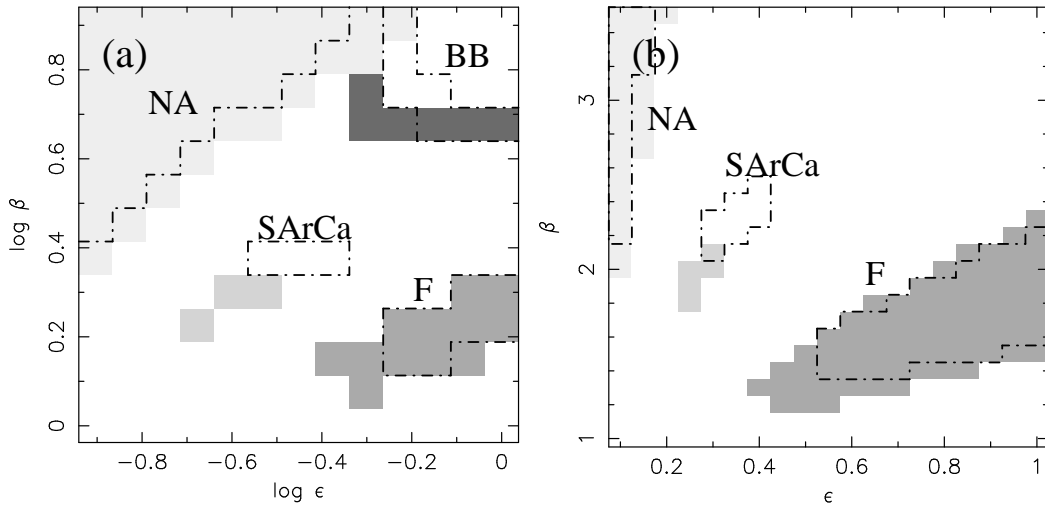
FIG. 7.— (a) A comparison between the region of allowed $\epsilon : \beta$ parameter space for M82 predicted by the scaled CC model (shaded regions) in comparison to the regions predicted by the full two-dimensional hydrodynamical simulations (regions enclosed by dot-dashed lines, previously shown in Fig. 5), using parameter set A. (b) As in (a), except the comparison uses the finer grid of models distributed linearly in a smaller region of $\epsilon : \beta$ parameter space.
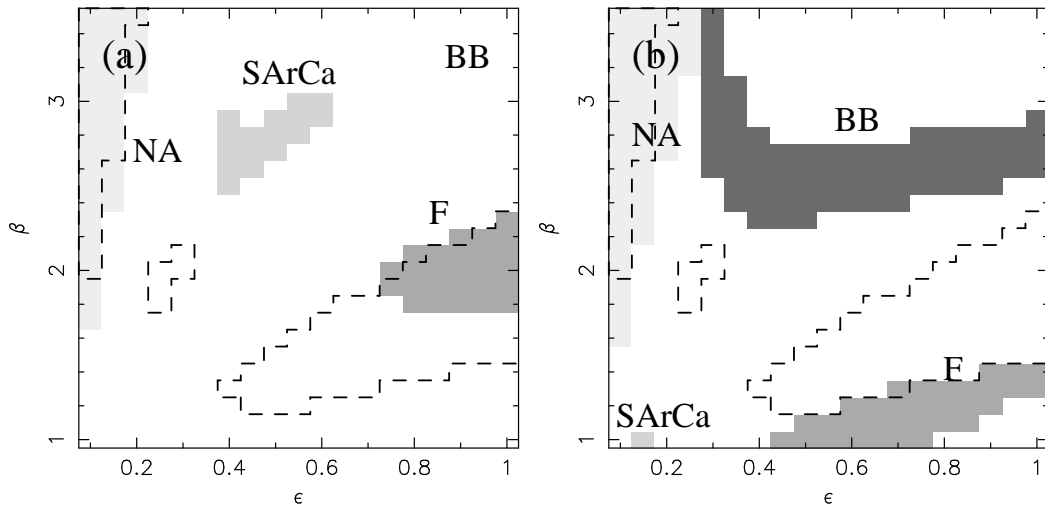

FIG. 8.— (a) A comparison between the region of allowed $\epsilon : \beta$ parameter space for M82 predicted by the scaled CC model using parameter set B (shaded regions) in comparison to the equivalent regions for parameter set A (dashed lines). (b) As in (a), except the comparison is between parameter set C and parameter set A. Parameter sets B and C differ from A in the assumed starburst star formation mode and age.

Parameter sets B through I are shown in Table 5. These alternate parameter sets explore the influence of the chosen star formation mode and age, starburst region size, supernova and stellar wind metal abundance, and participation factor on the region of allowed $\epsilon : \beta$ parameter space. All of these calculations were performed using the scaled CC model alone. Predicted central density, pressure and temperature, along with the terminal velocity, total cooling, broad-band hard X-ray ($E = 2 - 8$ keV band) luminosity and Fe Heα and S Lyα line luminosities for $\epsilon = 1$ and $\beta = 1$ are shown in Table 7.

Parameter set B differs from the previously discussed parameter set A only in that is assumes that ongoing star formation began 10 Myr ago, rather than 30 Myr ago. As the younger stellar population is intrinsically more luminous, less star formation is required to match the IR luminosity of M82 and consequently the mechanical energy and mass injection rates in parameter set B are lower than in parameter set A. Furthermore the ratio of energy to mass injection is lower, resulting in a lower central temperature of $T_c \sim 8 \times 10^7$ K for unit ϵ and β compared to $T_c \sim 10^8$ K in parameter set A, and a lower temperature than parameter set A for any given value of

ϵ and β. Cumulatively these differences result in a significant shift in the location of the the models in $\epsilon : \beta$ parameter space that match either the full or SArCa constraints (see Fig. 8a).

Generation of plots equivalent to Fig. 6 (not shown) reveals that the region matching the full set of constraints is again determined by the intersection of the Fe Heα and S Lyα observational constraints. Furthermore, at a given value of ϵ and β the predicted broad band and (in particular) line luminosities are lower for parameter set B than for parameter set A, with the least difference in luminosity occurring at $\epsilon = \beta = 1$.

Application of Equation 15 indicates that parameter set B yields emission integrals consistently ~ 0.1 dex lower than parameter set A for all values of ϵ and β. For the Fe and S lines the lower temperature of parameter set B when $\epsilon \sim \beta \sim 1$ results in a higher cooling function that offsets the reduced emission integral because the lower temperature is closer to the peak of the line-specific cooling functions, such that the predicted values of $L_{\mathrm{FeHe}\alpha}$ and $L_{\mathrm{SLy}\alpha}$ are comparable to those of parameter set A (Table 7). But over much of the $\epsilon : \beta$ parameter space the lower temperatures in parameter set B result in lower line emissivities that in combination with the
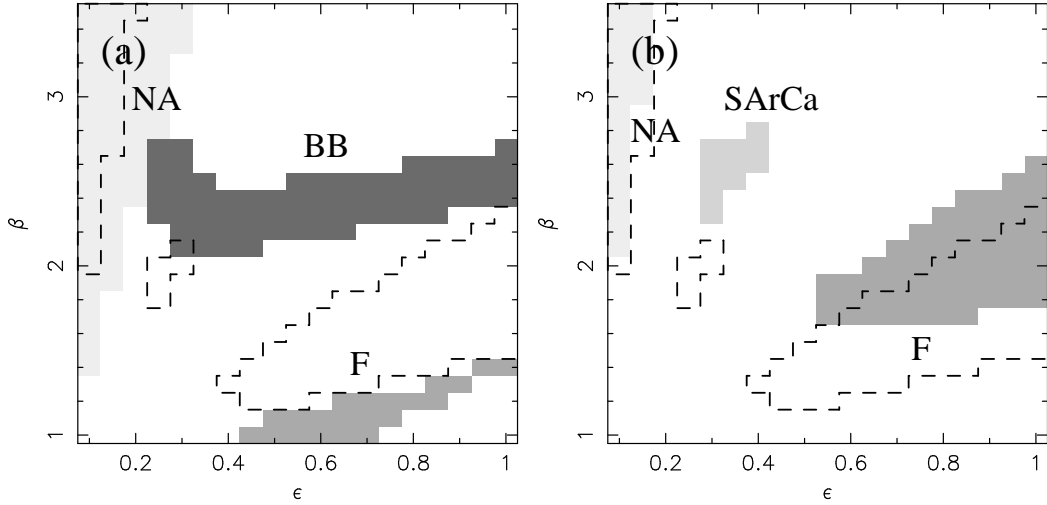
FIG. 9.— (a) A comparison between the region of allowed $\epsilon : \beta$ parameter space for M82 predicted by the scaled CC model using parameter set D (shaded regions) in comparison to the equivalent regions for parameter set A (dashed lines). (b) As in (a), except the comparison is between parameter set E and parameter set A. Parameter sets D and E differ from A in adopting respectively smaller and larger starburst effective radii $R_\star$.
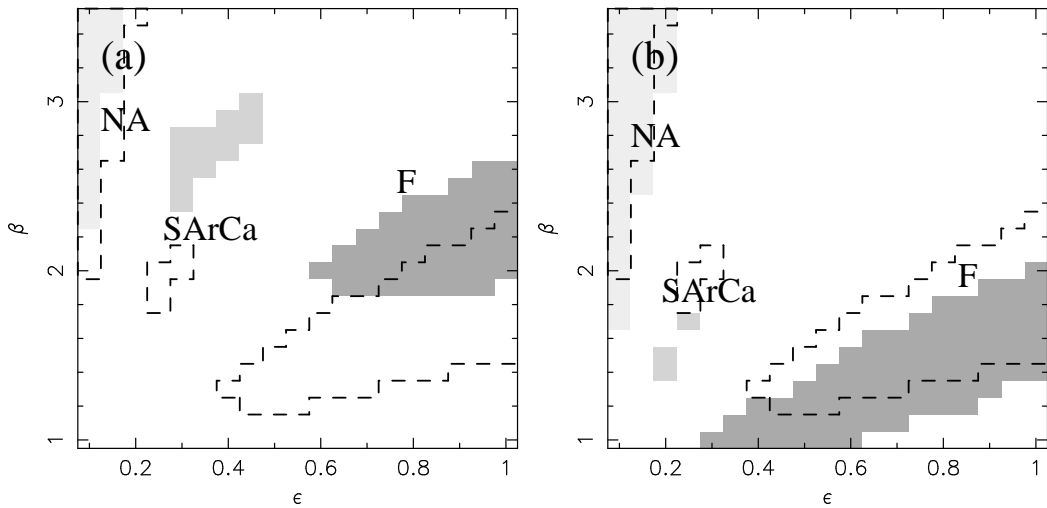

FIG. 10.— (a) A comparison between the region of allowed $\epsilon : \beta$ parameter space for M82 predicted by the scaled CC model using parameter set F (shaded regions) in comparison to the equivalent regions for parameter set A (dashed lines). (b) As in (a), except the comparison is between parameter set G and parameter set A. Parameter sets F and G differ from A in adopting respectively smaller and larger supernova and stellar wind metal abundances $Z_{\rm SN+SW}$.
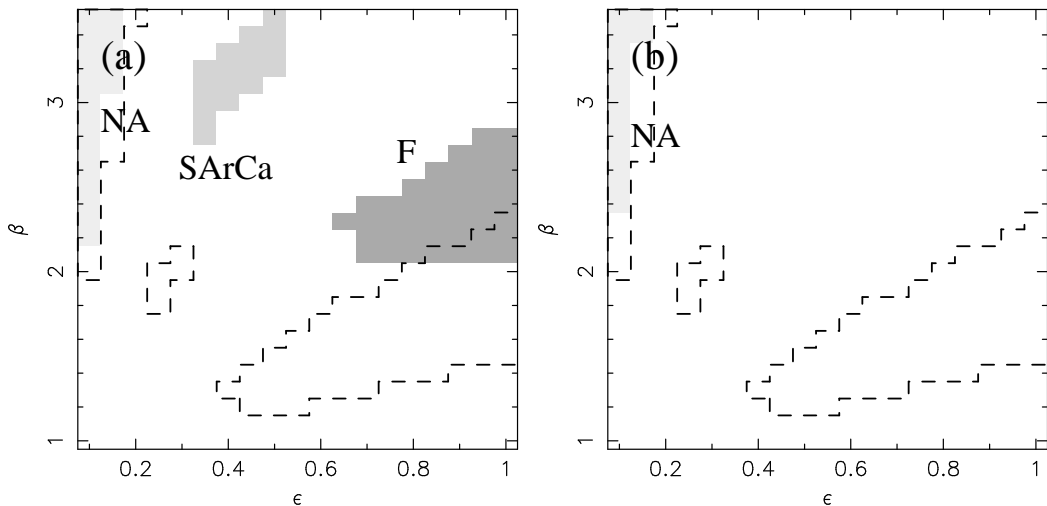

FIG. 11.— (a) A comparison between the region of allowed $\epsilon : \beta$ parameter space for M82 predicted by the scaled CC model using parameter set H (shaded regions) in comparison to the equivalent regions for parameter set A (dashed lines). (b) As in (a), except the comparison is between parameter set I and parameter set A. Parameter sets H and I differ from A in adopting lower values of the participation factor $\zeta = 0.71$ and $\zeta = 0.50$ respectively, i.e. effectively lower star formation rates.

TABLE 6
SUPERWIND PROPERTIES THAT MATCH THE FULL SET OF OBSERVATIONAL CONSTRAINTS.

Parameter Set	N_{match}	Range in parameter consistent with full constraints					
$\cdots$	$\cdots$	ϵ	β	$\log T_{\mathrm{c}}$	$\log P_{\mathrm{c}}/k$	$\log \dot{p}_{\mathrm{WF}}$	v_{∞}
(1)	(2)	(3)	(4)	(5)	(6)	(7)	(8)
A[a]	52	$0.55 - 1.0$	$1.4 - 2.2$	$7.56 - 7.82$	$7.15 - 7.38$	$34.31 - 34.54$	$1555 - 2097$
A	75	$0.40 - 1.0$	$1.2 - 2.3$	$7.51 - 7.84$	$7.08 - 7.40$	$34.23 - 34.55$	$1470 - 2164$
B	26	$0.75 - 1.0$	$1.8 - 2.3$	$7.49 - 7.66$	$7.13 - 7.24$	$34.29 - 34.39$	$1434 - 1745$
C	32	$0.45 - 1.0$	$1.0 - 1.4$	$7.64 - 7.87$	$7.22 - 7.47$	$34.37 - 34.62$	$1709 - 2239$
D	21	$0.45 - 1.0$	$1.0 - 1.4$	$7.67 - 7.87$	$7.80 - 8.05$	$34.20 - 34.44$	$1778 - 2240$
E	60	$0.55 - 1.0$	$1.7 - 2.6$	$7.48 - 7.76$	$6.94 - 7.17$	$34.35 - 34.58$	$1426 - 1976$
F	47	$0.60 - 1.0$	$1.9 - 2.6$	$7.50 - 7.72$	$7.26 - 7.43$	$34.41 - 34.58$	$1452 - 1874$
G	76	$0.30 - 1.0$	$1.0 - 2.0$	$7.50 - 7.87$	$6.96 - 7.37$	$34.11 - 34.52$	$1452 - 2240$
H	43	$0.65 - 1.0$	$2.1 - 2.8$	$7.47 - 7.70$	$7.15 - 7.29$	$34.30 - 34.44$	$1409 - 1829$
I	0	$\cdots$	$\cdots$	$\cdots$	$\cdots$	$\cdots$	$\cdots$

NOTE. — Column 1: Parameter set name. Column 2: N_{match} is the number of models that match the full set of observational constraints, out of the 494 models calculated for each parameter set. Columns 3 and 4: The range of thermalization efficiencies ϵ and mass loading factors β found to match the full set of observational constraints. The remaining columns show the range in a variety of physical properties of the M82 superwind found in the models that match the full set of observational constraints: central temperature T_{c} (column 5, in Kelvin), central pressure P_{c}/k (column 6, in units of K cm^{-3}), rate of change of superwind momentum $\dot{p}_{\mathrm{WF}} = \dot{M}_{\mathrm{tot}} \times v_{\infty}$ (column 7, units g cm s^{-2}) and wind terminal velocity v_{∞} (column 8, units km s^{-1}).
[a] Calculated using 2-dimensional hydrodynamical simulations. All other parameter sets were calculated using the scaled 1-dimensional Chevalier & Clegg model.

lower emission integral result in lower line luminosities than in parameter set A. Ultimately the regions in $\epsilon : \beta$ parameter space that match the full and SArCa constraints in parameter set B require higher mass loading and higher thermalization efficiency than in parameter set A in order to increase the emission integral without further decreasing the temperature. Increasing β strongly increases the net emission integral as $EI \propto \beta^3/\epsilon$, although it slightly decreases the plasma temperature (which must then be offset by increasing the thermalization efficiency). In contrast, reducing the thermalization efficiency is counter productive as the increase in EI is counteracted by the decrease in temperature that consequently reduces the line emissivities.

Parameter set C represents the star formation in the nucleus M82 as a single instantaneous burst occurring 10 Myr ago. Compared to parameter set A this results in a higher mechanical energy and mass injection rate, although the ratio of energy to mass injection is much closer to that in parameter set A than the lower values of parameter set B.

The higher mass injection for parameter set C leads to higher predicted X-ray luminosities for a given value of ϵ and β than for parameter set A, which has a significant effect on the regions of $\epsilon : \beta$ parameter space that match the various constraints (Fig. 8b). The region matching the $E = 2 - 8$ keV broad band luminosity appears at much lower β than in parameter set A, although in terms of absolute mass injection $\dot{M}_{\rm tot}$ the location of this region is consistent between parameter set A and parameter set C.

Similarly, lower values of β are required to match the full set of constraints, the allowed region extending between $0.4 < \epsilon \leq 1$ and $1 \leq \beta \lesssim 1.4$. Models with $\epsilon = \beta = 1$ are again excluded as possible matches to the observed properties of M82, but for different reasons than in the case of parameter sets A and B. For parameter set C models with $\beta \sim 1$ and $\epsilon \sim 1$ generate sufficient Fe Heα luminosity to match the required constraint, but these models predict a Fe Lyα/Heα line ratio greater than the upper limit of 0.34 (i.e. T_c is too high), and hence do not match the full set of constraints. A combination of constraints shapes upper edge of the allowed region. In addition to the requirement not to overproduce the S Lyα emission that we encountered with parameter sets A and B, the upper edge of the allowed region in parameter set C is also set where the Fe Heα luminosity exceeds the observational limits.

Parameter set D adopts the compact starburst region discussed in § 3.3.2. In terms of the effective radius of the starburst region parameter set D uses $R_\star = 125.5$ pc instead of $R_\star = 300$ pc, but is otherwise identical to parameter set A. Consequently the gas density within the starburst region ($n_c = 0.91\,{\rm cm}^{-3}$) is considerably higher than in parameter set A ($n_c = 0.16\,{\rm cm}^{-3}$) or even parameter set C ($n_c = 0.26\,{\rm cm}^{-3}$), and results in a significant increase in the X-ray emission despite the reduction in starburst region volume (see Equ. 15). The regions of $\epsilon : \beta$ parameter space over which parameter set D matches the various sets of constraints is very similar to that parameter set C (Fig. 9a) for the same reasons we discussed above. The region of $\epsilon : \beta$ parameter space that matches the full set of constraints is smaller than in parameter set C because of the greater increase in luminosity caused by the higher gas density, and no region of $\epsilon : \beta$ matches the SArCa constraints. It is possible that with tighter observational constraints on $L_{\rm FeHe\alpha}$ and $L_{\rm SLy\alpha}$ there would be no region of $\epsilon : \beta$ parameter space that would match the full set of

observational constraints.

The lower volume of the starburst region adopted in parameter set D also leads to higher central pressures. Models that match the full set of observational constraints have $7.80 \leq \log P_c/k \leq 8.05$, values that are $2 - 4$ times higher than the highest independent observational estimates of the thermal pressure in the core of M82. This leads us to suspect that parameter set D is not a valid physical representation on the M82 starburst.

Parameter set E adopts the largest of the possible starburst region geometries discussed in § 3.3.2, for which the effective radius is $R_\star = 406$ pc and the resulting central number density is $n_c = 0.09\,{\rm cm}^{-3}$. The region that matches the full set of observational constraints now moves toward higher ϵ and higher β with respect to the same region in parameter set A (Fig. 9b), for similar reasons to those we discussed regarding parameter set B. Increased mass loading is required to make up for the reduction in gas density due to the larger starburst, but the thermalization efficiency must also increase so as to maintain a central temperature that maximizes the Fe Heα emissivity ($7.5 \lesssim \log T_c \lesssim 7.8$, for parameter sets A, B and E. See Table 6).

In § 3.3.4 we discussed the expected metal abundance of the merged SN ejecta and stellar wind ejecta. The calculations of Limongi & Chieffi (2007) predict a higher iron abundance for the SN ejecta ($Z_{\rm Fe,SN} = 7Z_{\rm Fe,\odot}$) than the Starburst99 calculations that combine Woosley & Weaver (1995) SN yields with stellar wind ejecta ($Z_{\rm Fe,SN+SW} = 4Z_{\rm Fe,\odot}$). Furthermore the Limongi & Chieffi calculations predict that sulphur, argon and calcium are less enriched than iron, while Starburst99 predicts that sulphur is more strongly enriched than iron. In all of the calculations we have discussed until now we adopted a uniform relative enrichment of all elements, $Z_{\rm SN+SW} = 5Z_\odot$. Parameter sets F and G explore the influence of the adopted metal abundance on the region of $\epsilon : \beta$ parameter space that match the observational constraints: parameter set F adopts $Z_{\rm SN+SW} = 2.5Z_\odot$ while parameter set G adopts $Z_{\rm SN+SW} = 7.5Z_\odot$. Given the already large uncertainties in the yields we feel that exploring the effect of adopting different yields for different elements is beyond the scope of this paper.

The lower metal abundance in parameter set F leads to lower lower S, Ar, Ca and Fe line luminosities than for parameter set A. For $\beta = 1$ the line luminosities are exactly half those in parameter set A, but the fractional difference becomes less as β increases and the influence of the mass-loaded material on the net metal abundance of the wind fluid $Z_{\rm WF}$ becomes larger (Equ. 12). The result in terms of the region of $\epsilon : \beta$ parameter space that matches the observational constraints is shown in Fig. 10a, and is very similar to that in parameter sets B and E that also generate lower line luminosities for different reasons.

Conversely the higher metal abundance in parameter set G leads to higher line luminosities than parameter set A, although they are generally less than those in parameter sets C and D (see e.g. Table 7). The $\epsilon : \beta$ region of matches is shown in Fig. 10b. The upper β edge of the region that matches the full set of observational constraints is set by the upper limit on the S Lyα luminosity, while the lower β edge of this region is set by a combination of the Fe Lyα/Heα line ratio constraint and the minimum acceptable Fe Heα line luminosity.

Parameter sets H and I explore the effect of varying the participation fraction ζ (see § 3.3.3). Reducing ζ has the effect of reducing the effective star formation rate without altering the energy per particle, and the emission integral and lumi-

nosities for a given value of ϵ and β are equal to those from parameter set A except multiplied by a factor ζ^2. For parameter set H, where $\zeta = 2^{-1/2}$, the factor 2 reduction in all luminosities moves the regions that match both the SArCa and full set of constraints to higher β and higher ϵ (Fig. 11a). Parameter set I has $\zeta = 0.5$ and the reduction in luminosity is so significant that the region matching the SArCa constraints has moved off of the region shown in Fig. 11b to $0.5 \lesssim \epsilon \lesssim 0.9$, $4.5 \lesssim \beta \lesssim 5.5$. More significantly, there are no values of ϵ or β that can match the full set of observational constraints when using parameter set I.

5. DISCUSSION

In Strickland & Heckman (2007) we concluded that the diffuse Fe Heα emission from the central ~ 500 pc of M82 could have been produced by thermalized SN ejecta and stellar wind material from the starburst based on relatively simple estimates of the plasma properties of the emitting material.

The more rigorous approach to the interpretation of the diffuse hard X-ray emission taken in this paper strengthens that conclusion: the plasma responsible for the hard X-ray iron-line emission is the same gas that drives the larger-scale superwind in this starburst galaxy. Furthermore our method allows us to make quantitative statements regarding supernova feedback and the properties of M82's starburst-driven superwind.

5.1. Supernova Thermalization (Heating) Efficiencies and Mass Loading

The primary aim of this paper was to establish what constraints could be made on the efficiency of supernova heating and the net rate of mass injection within a starburst region.

It is generally accepted that in more normal, or quiescent, star forming galaxies such as the Milky Way on average only $\sim 10\%$ of the 10^{51} erg of initial kinetic energy per supernova ends up heating or moving the ISM, with the remainder being lost as radiation (see e.g. Thornton et al. 1998; Efstathiou 2000). Although it had long been suspected that the efficiency of supernova heating is a function of the local interstellar and star forming conditions there was no direct method by which to measure this thermalization efficiency in a starburst galaxy until, as described in § 1, the launch of the *Chandra* X-ray Observatory.

Theoretical arguments have been made for either lower or higher SN heating efficiencies in more actively star-forming galaxies. Steinmetz & Navarro (1999) argued that radiative energy losses must always be severe because massive stars form in regions of high gas density. In contrast Heckman et al. (1990) argue that thermalization must be efficient in starbursts because a high supernova rate per unit volume leads to an increased filling factor of the hot low density ISM, which in turn reduces the radiative energy losses experienced by subsequent SNe. Thus the SN thermalization efficiency depends on the SN-modulated porosity of the ISM (e.g. McKee & Ostriker 1977). Recent numerical simulations by Melioli & de Gouveia Dal Pino (2004) appear to qualitatively demonstrate such a time-dependent non-linear thermalization efficiency. Intriguingly they find that the thermalization efficiency (which they term the heating efficiency) can only be low ($\lesssim 10\%$) or very high ($\sim 100\%$) for any significant period of time, transitioning between to two states very rapidly.

Let us briefly review how the hard X-ray line emission from a starburst region is related the average thermalization

efficiency ϵ and the mass loading factor β. Both of these parameters strongly affect the net volume emission integral $EI \propto \beta^3/\epsilon$ (Equation 15) and the line emissivities $\Lambda(T,Z)$ through the plasma temperature $T \propto \epsilon/\beta$ (Equation 8, Fig. 4) and the metal abundance of the wind fluid Z_{WF} (Equation 12).

In the specific case of M82 it is the Fe Heα and S Lyα lines that drive the allowed values of ϵ and β we derive. For many of the sets of model parameters we have explored it should be noted that $\epsilon = \beta = 1$ will not reproduce the observed constraints because too little Fe Heα emission is produced as the plasma density within the starburst region is too low. Thus successful models must have a higher volume emission integral which implies $\beta > 1$ and/or $\epsilon < 1$.

As we described in § 4.1, the lower boundary of acceptable mass loading factors β for a given value of the thermalization efficiency ϵ is set by requirement to achieve sufficient Fe Heα emission ($37.96 \leq \log L_{\mathrm{FeHe\alpha}} \leq 38.39$), while the maximum β is set by the requirement not to exceed the observed S Lyα luminosity ($\log L_{\mathrm{SLy\alpha}} \leq 37.43$).

Furthermore the central temperature (and hence ϵ/β) must be high enough that the Fe Heα emissivity is significant with respect to the emissivity of the lower ionization lines, in particular the sulphur lines. This constraint ultimately controls the minimum allowed value of the thermalization efficiency ϵ, and is the reason why the different parameter sets tend to have similar minimum values of T_c, specifically $\log T_c \gtrsim 7.5$ (see Table. 6).

The central temperature can not exceed 7.8×10^7 K ($\log T_c = 7.9$) as otherwise the upper limit on the Fe Lyα/Heα line ratio would be violated. For a given value of ϵ this constraint determines the lowest allowed values of β in cases where the Fe Heα luminosity is sufficiently high enough to match the observational constraints. This upper temperature constraint is only significant when the model parameters generate higher central densities or luminosities (more mass injection, a more compact starburst, or a higher metal abundance in the ejecta), and thus there is a broader range in the maximum allowed T_c than in the minimum allowed T_c.

Returning to the consideration of our results, we find that for all parameter sets that produce at least one valid solution that can match the full set of observational constraints for M82, those valid solutions always include thermalization efficiencies of 100%.

Furthermore ϵ is never less that 30%, and over the range of parameter sets we have explored the minimum valid thermalization efficiency ϵ_{min} ranges from 30% to 75% (see Table 6). Within this range there is a small degree of variation associated with different starburst model parameters we have explored. We find that the starburst history and ejecta metal abundance $Z_{\mathrm{SN+SW}}$ have some effect on the allowed thermalization efficiency, while the starburst region size appears to have little influence on the minimum allowed thermalization efficiency (Table 6). For example in a younger continuous star formation (CSF) model for the burst (parameter set B) the minimum allowed thermalization efficiency is $\epsilon_{\mathrm{min}} = 0.75$ in comparison to the older CSF we adopt as the default starburst history ($\epsilon_{\mathrm{min}} = 0.4$) or the single instantaneous burst model (parameter set C, $\epsilon_{\mathrm{min}} = 0.45$).

That ϵ must be $\gtrsim 30\%$ is a striking result. If the diffuse $E \sim 6.7$ keV iron line in M82 arises in a collisional plasma then the average thermalization efficiency in the M82 starburst region can be as high as 100%, while it can not be as low as 10%. Our results give quantitative support to the arguments presented by Heckman et al. (1990) and Melioli & de Gouveia Dal Pino

TABLE 7
STARBURST REGION PROPERTIES FOR $\epsilon = 1$ AND $\beta = 1$.

Parameter Set ... (1)	$\log n_c$ ... (2)	$\log P_c/k$ ... (3)	$\log T_c$ ... (4)	v_∞ ($\mathrm{km\,s^{-1}}$) (5)	r_{12} (pc) (6)	$\log L_{tot}$ ... (7)	$\log L_{2-8keV}$ ... (8)	$\log L_{FeHe\alpha}$ ... (9)	$\log L_{SLy\alpha}$ ... (10)
A	-0.80	7.22	8.02	2651	278	38.67	38.27	37.46	36.22
B	-0.85	7.06	7.91	2341	278	38.56	38.17	37.45	36.24
C	-0.59	7.40	7.98	2548	285	39.09	38.70	37.92	36.69
D	-0.04	7.98	8.02	2651	121	39.17	38.75	37.93	36.74
E	-1.06	6.96	8.02	2651	369	38.49	38.09	37.27	35.98
F	-0.80	7.22	8.02	2651	278	38.51	38.11	37.16	35.92
G	-0.80	7.22	8.02	2651	278	38.80	38.39	37.64	36.40
H	-0.95	7.07	8.02	2651	272	38.37	37.97	37.16	35.92
I	-1.10	6.92	8.02	2651	266	38.07	37.67	36.86	35.62

NOTE. — Column 1: parameter set name. Columns 2, 3 and 4: Logarithms of the central number density ($\mathrm{cm^{-3}}$), the central pressure divided by Boltzmann's constant, and the central temperature (K) respectively for models where $\epsilon = 1$ and $\beta = 1$. Column 5: Wind terminal velocity. Column 6: The radius at which the ionization parameter η (see Equation 14) drops below $10^{12}\,\mathrm{cm^{-3}}$ s. Columns 7, 8, 9 and 10: Logarithms of the plasma luminosity ($\mathrm{erg\,s^{-1}}$) within a radius of 500 pc. Columns are the total cooling luminosity, the $E = 2 - 8$ keV energy band X-ray luminosity, the Fe Heα line luminosity and the S Lyα line luminosity respectively.

(2004) for a higher thermalization efficiency in starbursts than in normal star-forming galaxies. The issue of whether the thermalization efficiency must be 100%, or whether high but intermediate values are allowed, remains an interesting but open question.

With respect to the mass-loading of the superwind in M82 we find that the majority of the parameter sets we have considered require some centralized mass loading of the wind fluid, although at low-to-moderate levels. Over all parameter sets $1 \leq \beta \leq 2.8$, but only parameter sets C, D and G allow $\beta = 1$ and more typically $1.5 \lesssim \beta \lesssim 2.5$.

Parameter sets C, D and G allow zero additional mass-loading ($\beta = 1$) as a valid solution when coupled with lower values of the thermalization efficiency ($\epsilon \sim 30 - 70\%$). In parameter set C this is because the single instantaneous starburst injects more mass than the constant star formation model used in the other parameter sets, and hence does not require additional sources of mass to increase the plasma density within the starburst region. In parameter sets D and G the non-mass-loaded plasma within the starburst region is sufficiently luminous without additional mass-loading because of either the compactness of the starburst (D), or the higher metal abundance (G), increases the net luminosity. High values of ϵ are excluded as valid solutions when $\beta = 1$ for these three parameter sets because the high central plasma temperature violates the Fe Lyα/Heα line ratio constraints.

Thus these results suggest that it is plausible that the raw SN and stellar wind ejecta from the massive stars in M82's starburst have been efficiently mixed with a roughly equivalent mass of initially cooler ambient gas, although no mass loading is also a possible solution. The net effect is an average mass outflow rate from the starburst region in the very hot phase of the wind fluid of $\dot{M}_{tot} \sim 2.5\,M_\odot\,\mathrm{yr^{-1}}$, approximately half of the gas consumption due to the star formation rate alone (§ 3.3.1). The allowed range of wind fluid outflow rate covering all parameter sets except parameter set D lies in the range $1.4 \lesssim \dot{M}_{tot}(M_\odot\,\mathrm{yr^{-1}}) \lesssim 3.6$ (a fraction $\sim 0.3 - 0.8$ of the star formation rate for the Salpeter IMF we adopt).

This level of mass-loading is significantly lower than the values others have derived from soft X-ray observations of superwinds. Suchkov et al. (1996) used fairly sophisticated 1-dimensional hydrodynamical modeling to estimate that a mass-loading factor of $\beta \sim 3 - 6$ was required in to match the

soft X-ray properties of M82 known at that time from *Einstein* and *ROSAT* HRI observations. For the dwarf starburst galaxy NGC 1569 Martin et al. (2002) estimated $\beta \sim (8 - 35) \times \eta^{1/2}$ (where η is the volume filling factor of the X-ray-emitting plasma) based on the estimated mass of soft X-ray-emitting gas seen in *Chandra* observations. Grimes et al. (2007) derived a value of $\beta \sim 5\,\eta^{1/2}$ for the soft X-ray-emitting plasma in the local Lyman Break Galaxy analog Haro 11. Both Martin et al. and Grimes et al. obtain similar estimates of β based on the best-fit metal abundances in the soft X-ray-emitting plasma compared to the expected abundances of a SN-ejecta-enriched plasma (see Equation 12).

However a direct comparison between our findings and the existing results in the literature is somewhat misleading.

The results from the literature are all based on soft X-ray observations of starbursts that probe gas in the temperature range 2 – 10 million K, not the hotter 30 – 70 million gas probed by the observations of M82's diffuse hard X-ray emission. The high mass loading factors simply reflect the fact that there is more mass in the soft X-ray emitting plasma than can be accounted for by SN and stellar wind ejecta alone.

Soft X-ray mass loading factors are further based on measurements that cover the entire soft X-ray nebula associated with the target starburst galaxy (over ~ 5 kpc-scales for M82 and Haro 11, and over ~ 1 kpc in NGC 1569), whereas our measurement constrains the mass loading of the wind fluid within the ~ 500 pc starburst region itself (in the terminology introduced by Suchkov et al. (1996) this is central mass loading). It is plausible that the wind fluid experiences additional mass-loading as it flows outward beyond the starburst region (distributed mass loading).

The older measurements referred to above can not differentiate between a localized or a global mass-loading process (by global we mean a process that is essentially volume filling), although we have previously argued that a significant fraction of the soft X-ray emission must arise from a low-volume filling factor component of the wind (Strickland et al. 2000, 2002, 2004a). In contrast the mass loading factor derived in this paper is for a volume-filling mass loading.

It is worth noting that it is not the case that the hottest plasma in a superwind is necessarily also the least mass-loaded phase. The technique we have presented could detect a mass loading factor of $\sim 5 - 10$ for the very hot gas in the

starburst region. The line luminosities are strong functions of the mass loading factor (Fig. 5), so that both the Fe and S line emission would be more intense than observed in the case of a higher mass-loading factor. Both low thermalization efficiency and high mass loading are more readily observable. In a sense it is the relative faintness of these lines from M82 that force us toward the allowed values of the thermalization efficiency and mass loading factor given in Table 6. Even if part of the starburst region experienced higher mass loading than another part our final estimate of the allowed mass loading factor would be skewed toward the higher value as β is essentially luminosity-weighted. Thus we conclude that the $T \gtrsim 3 \times 10^7$ K component of M82's superwind (the wind fluid) genuinely has a relatively low degree of mass-loading within the starburst region.

5.2. *Physical Properties of the M82 Starburst*

Despite the broad range of input model parameters we have explored in the various parameter sets we find that the physical properties of the base of the M82 superwind in the allowed models are all relatively similar (Table 6).

We have already described the relatively narrow allowed range for the central temperature, $7.5 \lesssim \log T_c \lesssim 7.9$, and the physical constraints that drive this result. The result is all the more notable given the relatively poor constraints provided by the traditional line-ratio diagnostics shown in Table 2.

Similarly the central pressure and wind momentum injection rate are constrained to lie within a range of ~ 0.5 dex ($7.0 \lesssim \log P_c/k \lesssim 7.5$, $34.1 \lesssim \log \dot{p}_{WF} \lesssim 34.6$), if we exclude parameter set D from consideration because of its unrealistically high pressure. These pressures are in good agreement with independent estimates of the thermal pressure within the ISM in the starburst region, as previously discussed.

The momentum injection rate is an important parameter with regard to the acceleration of the WNM and WIM by the wind fluid (see e.g. Heckman et al. 1990, 2000)[9]. By way of comparison the momentum injection rate assuming 100% thermalization efficiency and no mass loading is $\log \dot{p}_{WF} = 34.2$ for the star formation models adopted in parameter sets A and B, and $\log \dot{p}_{WF} = 34.6$ for parameter set C. Thus taking account of imperfect thermalization and additional (central) mass loading does not significantly alter the M82 starburst momentum injection rate from the values one would estimate from SNe and stellar winds alone.

5.3. *Characteristic Velocities of the M82 Superwind*

The moderately tight limits on the central temperature we have derived also make for tight limits on the terminal velocity of the wind fluid, as $v_\infty \propto T_c^{1/2}$ (Equation 11). Over all the parameter sets, models that match the full set of the observational constraints predict v_∞ in the range $1410 - 2240$ km s^{-1}.

This estimate of v_∞ is significantly higher than previous estimates of the terminal velocities in local starbursts (including M82) based on the temperature of the soft X-ray emitting gas, $v_{\infty,SX} = 440 \times (kT_{SX}/0.25\,\mathrm{keV})^{1/2}$ km s^{-1} (see e.g.

Martin 1999; Heckman et al. 2000; Martin 2005). However, it has been long understood that these estimates were effectively lower limits on v_∞ given the technical difficulties associated with robustly detecting a hotter and more tenuous (and thus intrinsically fainter) component of the wind.

Strictly speaking the terminal velocity is the characteristic velocity the wind fluid would asymptote to once outside the starburst region, if it expanded into a vacuum (see Fig. 3). For a superwind expanding into a gaseous medium there are additional characteristic velocities, some of which are phase-dependent (Strickland & Stevens 2000, Strickland & Dinge, in preparation), but all are less than or equivalent to v_∞. Nevertheless v_∞ remains an accurate measure of both the effective energy per particle of the most metal-enriched gas and the maximum velocity attainable by gas in a pressure-driven superwind.

For a wind that has broken-out of both the gaseous disk and halo of its host galaxy a comparison between v_∞ and the local escape velocity from the gravitational potential v_{esc} should give a qualitative indication of whether the material in the wind can escape.

Estimates of M82's escape velocity (and mass) have surprisingly large uncertainties for such a well-studied galaxy, because of its very unusual rotation curve and the possibility that its encounter with M81 has stripped it of its dark matter halo (Sofue 1998). The extreme options are a potential dominated by either a central mass within a radius of ~ 2 kpc or a dark matter halo extending out to 100 kpc, the two of which crudely limit the escape velocity to lie in the range $v_{esc} \sim (1.5 - 3.5) \times v_{rot}$. For a peak rotational velocity of $v_{rot} \sim 130$ km s^{-1} at a radius of ~ 500 pc (Götz et al. 1990), the escape velocity is $v_{esc} \sim 200 - 460$ km s^{-1}, much lower than the allowed range of $v_\infty = 1410 - 2240$ km s^{-1}.

Our estimated terminal velocity for M82's wind is also much larger than estimates of the velocity of the Hα emitting warm ionized medium, which achieves a maximum inclination-corrected velocity of $v_{H\alpha} \sim 600 - 650$ km s^{-1} at heights between $|z| \sim 350$ to 2000 pc from the nucleus (McKeith et al. 1995; Shopbell & Bland-Hawthorn 1998). This is not surprising, as the Chevalier & Clegg (1985) model predicts a large difference between the velocities of the wind fluid and the velocity of the WIM (which they identified as clouds of cooler denser gas entrained and accelerated by the wind fluid). In the case of M82 velocity of the WIM component of the wind appears to exceed the galactic escape velocity, although more generally the WNM and WIM in superwinds has a speed more closely comparable to v_{esc} and hence its long term fate is ambiguous (Heckman et al. 2000; Martin 2005).

Our results constrain the energy per particle within the starburst region, neglecting the possibility of radiative energy losses and additional mass-loading of the wind fluid exterior to the starburst region. Is it plausible that these effects could be of sufficient magnitude to reduce the terminal velocity of the wind fluid at large radius to a value below the escape velocity? For a starburst with a SN thermalization efficiency of $\epsilon = 0.3$ and a central mass loading factor $\beta = 1$ the larger scale wind would have to lose $\sim 90\%$ of its remaining energy to reduce the final value of v_∞ to 460 km s^{-1} in the absence of additional mass loading of the wind fluid (98% energy loss to reduce v_∞ to 200 km s^{-1}). The required energy loss fraction is very similar for a central starburst with $\epsilon = 1$ and $\beta = 2.3$. We know that radiative energy losses in M82's large-scale wind are small, $\lesssim 10\%$ (Hoopes et al. 2003;

---

[9] The terminal velocity of a cloud of radius and mass R_{cloud} and M_{cloud}, initially exposed to a radially-expanding SN-driven wind at a radius R_i from the origin, is proportional to $(\dot{p}_{WF}/R_i \times R_{cloud}^2/M_{cloud})^{1/2}$. Notably the terminal velocity of the cloud can be lower than the terminal velocity of the wind. For a radiation-pressure driven cloud the final result is essentially the same, with the substitution of $\dot{p}_{rad} = L_{BOL}/c$ for $\dot{p}_{WF}$. Clouds of entrained material are effectively momentum-driven irrespective of whether they are in an energy-driven hot wind or a radiation-driven wind.

Strickland et al. 2004b). It seems unlikely that the wind fluid could so effective in transferring enough of its energy to a different gaseous phase, such as the galactic halo medium, without a significant fraction of this energy being radiated and hence observed, unless the radiation is spread over a region much larger than the currently studied ~ 12 kpc extent of M82's wind. The remaining alternative is to strongly mass load the wind fluid once it has left the starburst region. Assuming that energy losses in the wind fluid are negligible then in the case of the starburst with $\epsilon = 0.3$ and $\beta = 1$ we would need to effectively mix an additional $\dot{M}_{\text{extra}} \sim 13\, M_\odot\, \text{yr}^{-1}$ into the wind fluid outside the starburst region to reduce v_∞ to $460\, \text{km s}^{-1}$ ($\sim 70\, M_\odot\, \text{yr}^{-1}$ to reduce v_∞ to $200\, \text{km s}^{-1}$). For $\epsilon = 1$ and $\beta = 2.3$ then $\dot{M}_{\text{extra}} \sim 43\, M_\odot\, \text{yr}^{-1}$ ($v_\infty = 460\, \text{km s}^{-1}$) and $\sim 240\, M_\odot\, \text{yr}^{-1}$ ($v_\infty = 200\, \text{km s}^{-1}$). Even the smallest of these values is uncomfortably large in terms of the required gas reservoir, and furthermore the resulting X-ray emissivity of the volume filling wind fluid might then exceed the observed soft X-ray luminosity of the wind ($EI \propto \dot{M}^3$). Given the preceding arguments we believe that is probable that the metal enriched wind fluid will ultimately escape M82.

5.4. *Implications for Understanding Feedback and Superwinds*

It is worth stressing that a multi-phase wind model leads to phase-dependent ejection efficiencies for the material in starburst-driven superwinds. Current cosmological models of galaxies that attempt to include superwinds invariably have single phase winds (although the simulation may allow multiple ISM phases, their galactic winds lack the fine-scale multiphase nature of real winds). Cosmological simulations lack the ability to separately model the differential ejection of the metal-enriched high-energy-per-particle wind fluid from the less enriched, lower velocity, but more massive WNM and WIM. Their results on metal transport and feedback processes in galaxies are potentially misleading or incorrect.

In particular, simulations that add all the gas mass of the WNM and WIM phases to the metal-enriched SN ejecta require nonphysically large fractions ($\epsilon \gtrsim 100\%$) of all the available SN mechanical energy in star-forming galaxies (normal galaxies in addition to starburst galaxies) in order to match the observed degree of metal loss from galaxies and metal enrichment of the IGM. (e.g. Springel & Hernquist 2003b; Oppenheimer & Davé 2006; Kobayashi et al. 2007). These papers interpret such problems as implying the physical inadequacy of purely SN-driven winds and need for addition energy or wind sources (e.g. radiation-driven winds). Our interpretation is that the flaw lies in the inadequacy of their recipe for winds. In contrast simulations that effectively treat the SN ejecta alone without additional WIM/WNM mass loading achieve good matches to observed Lyα and O VI absorber statistics while using reasonable SN efficiencies ($\epsilon \sim 30\%$, Cen et al. 2005; Cen & Ostriker 2006; Cen & Fang 2006).

We further note that it is unrealistic to apply a single uniform feedback prescription to all star forming galaxies. As discussed previously there are good reasons to expect that ϵ is a function of the local intensity of star formation. Furthermore only galaxies with average star formation rates[10]

---

[10] This value for the critical Σ_{SF} is based on a Salpeter IMF with mass limits of 1 and 100 $M_\odot$. Dahlem et al. (2006) demonstrate that the star formation intensity threshold to establish extra-planar gaseous activity depends on the host galaxy mass, but as this mass dependence is relatively weak we have ignored it in presenting the simple superwind recipe.

per unit area $\Sigma_{\text{SF}} \gtrsim 4 \times 10^{-2}\, M_\odot\, \text{yr}^{-1}\, \text{kpc}^{-2}$ show evidence for superwinds (Lehnert & Heckman 1996b; Heckman 2003; Dahlem et al. 2006).

In the spirit of Martin (1999) we now present a simplified bimodal feedback and superwind recipe appropriate for use in semi-analytical and numerical simulations of galaxy formation. This recipe is most applicable to simulations that aim to answer questions regarding the galaxy mass-metallicity relationship, and/or the metal content of the IGM, as it primarily addresses the metal-enriched stellar wind and SN ejecta from starburst-driven superwinds.

The formulation presented below differs from most currently used recipes for winds. It prevents massive galaxies with moderate star formation rates (such as the Milky-Way) and the bulk of the galaxy population at low redshift from having any wind-related metal-loss, but the chances of metal ejection from intensely star-forming galaxies (starbursts) is enhanced. It is unlikely to act as an effective mechanism to suppress star formation in all star-forming galaxies, unlike the wind recipes in the simulations we criticized earlier.

In galaxies with average star formation rates per units area greater than $\Sigma_{\text{SF}} \geq 4 \times 10^{-2}\, M_\odot\, \text{yr}^{-1}\, \text{kpc}^{-2}$ (i.e. starbursts) feedback is efficient and leads to the creation of galactic superwinds. The hot gas in a superwind can be characterized by a mass injection rate $\dot{M}_{\text{hot}}$ of material of metal abundance Z_{hot}, with an associated mechanical energy injection rate $\dot{E}_{\text{hot}}$. In terms of the star formation rate $\mathcal{S}$ in units of $M_\odot\, \text{yr}^{-1}$ for a Salpeter IMF between the mass limits of 1 and 100 $M_\odot$, then:

- $\dot{M}_{\text{hot}} \approx 0.3 \times \beta_{\text{hot}} \zeta\, \mathcal{S}\, M_\odot\, \text{yr}^{-1}$, where β_{hot} is in the range $1.0 - 2.8$.

- Z_{hot} is given by Equation 12, and is a function of the metal abundance in the merged SN and stellar wind eject $Z_{\text{SN+SW}}$, the metal abundance in the cool ambient ISM Z_{cold} and the mass loading factor β_{hot}.

- The effective mechanical energy injection rate, accounting for the efficiency of thermalization, $\dot{E}_{\text{hot}} \approx 6.5 \times 10^{41} \epsilon_{\text{hot}} \zeta\, \mathcal{S}\, \text{erg s}^{-1}$, where ϵ_{hot} is in the range $0.3 - 1.0$.

- Alternatively, if winds are implemented by imparting a fixed velocity to gas "particles," then the appropriate velocity is $v_{\text{hot}} \approx 2650\, (\epsilon_{\text{hot}}/\beta_{\text{hot}})^{1/2}\, \text{km s}^{-1}$, and should be in the range $1400 - 2200\, \text{km s}^{-1}$.

- The values of ϵ_{hot} and β_{hot} are correlated in the sense that low values of ϵ are associated with low values of β, such that T_c or v_∞ lie in the range described in § 5.1 & 5.3.

- The participation factor ζ is the fraction of the total star formation that can effectively participate in driving a superwind. In the case of M82 ζ is unlikely to be lower than ~ 0.5, and is more plausible in the range $\zeta \sim 0.7 - 1.0$ (see Appendix C).

In more quiescent star forming galaxies with $\Sigma_{\text{SF}} < 4 \times 10^{-2}\, M_\odot\, \text{yr}^{-1}\, \text{kpc}^{-2}$ feedback is energetically inefficient and no true wind arises, although SN-heated and enriched gas may vent into the halo to form a galactic fountain. Galactic fountains are considerably less constrained theoretically than superwinds, but it is plausible that all the material eventually returns to the galactic disk after some delay.

This recipe captures two essential inter-related features of starburst and feedback physics that have been established in the local Universe and that have not been applied in existing recipes for winds in cosmological simulations: the existence of a threshold in star formation activity per unit disk area necessary to drive global galactic winds, and that the quantitative properties of feedback are not the same in all galaxies but depend on the intensity of star formation.

5.5. *Measuring feedback parameters in other starburst galaxies*

One limitation of the superwind recipe as presented is that it treats all starbursts equally, and applies an M82-like wind to them all. Although simulations of the type made by Melioli & de Gouveia Dal Pino (2004) suggest that the efficiency of supernova feedback may be bimodal, other evidence suggests that not all starburst-driven flows are equally energy-efficient (see e.g. Calzetti et al. 2004).

The techniques described in Strickland & Heckman (2007) and in this paper can be applied to other starburst galaxies in order to measure their effective supernova thermalization efficiencies and mass-loading parameters. In general one would be limited to a purely spectral X-ray analysis, as for more distant starbursts it would be difficult to spatially separate the hard diffuse X-ray emission from the emission from X-ray binaries and nuclear AGN even with the *Chandra* X-ray Observatory.

If our model is correct then we expect that the luminosity of the diffuse hard X-ray (HX) emission of a starburst region of star formation rate $\mathcal{S}$ and effective radius $R_\star$ to scale roughly as

$$L_{HX} \propto EI \times \Lambda \propto \frac{\beta^3 \zeta^2}{\epsilon} \frac{\mathcal{S}^2}{R_\star}, \qquad (16)$$

where we have substituted the star formation rate into Equation 15, and have ignored the ϵ and β dependence of Λ.

This is notable as it predicts L_{HX} from the wind fluid has a stronger than linear dependence on the star formation rate. It should therefore be possible to extract this emission component from the other hard X-ray emission components in star forming galaxies that have been shown to scale linearly with star formation rate (Ranalli et al. 2003; Grimm et al. 2003; Colbert et al. 2004; Persic & Rephaeli 2007). The task will also be simplified in that it is the hard X-ray line emission that has proven itself to provide the strongest constraints on ϵ and β in M82, rather than the hard X-ray continuum emission that the X-ray binaries dominate in the integrated X-ray spectra of galaxies.

We note that Fe Heα emission has been detected in the X-ray spectra of the nearby starburst NGC 253 (Weaver et al. 2002), the merging system Arp 299 (Ballo et al. 2004), and the ultra luminous IR galaxies (ULIRGs) Arp 220 (Iwasawa et al. 2005), Mrk 273 (Balestra et al. 2005), NGC 6240 (Netzer et al. 2005) and the Superantennae (Braito et al. 2008, submitted). Previously this emission has been interpreted in terms of ionized reflection associated with an AGN (Ross & Fabian 2005), and while this is likely true in objects with strong AGN (e.g. NGC 6240), ionized reflection might not be the cause of the Fe Heα emission in all of these objects. These papers often do consider a starburst origin for the ionized iron emission, but dismiss it based on the expectation that its luminosity should scale linearly with the star formation rate.

Apparently diffuse hard X-ray emission has also been seen in the *Chandra* observations of the starburst galaxies NGC 2146 (Inui et al. 2005) and NGC 3256 (Lira et al. 2002), although these papers do not discuss hard X-ray line emission. The *XMM-Newton* X-ray spectrum of NGC 3256 presented as Figure 2 of Jenkins et al. (2004) shows a hint of a hard X-ray iron line, but the paper does not quantify the energy and intensity of the feature.

To crudely test the plausibility of a wind fluid origin for the Fe Heα emission in these other starbursts we consider NGC 253 ($L_{FeHe\alpha} = (5.3^{+3.9}_{-2.8}) \times 10^{37}\,\mathrm{erg\,s^{-1}}$, Weaver et al. 2002), Arp 299 ($L_{FeHe\alpha} = (9.5 \pm 4.5) \times 10^{39}\,\mathrm{erg\,s^{-1}}$, Ballo et al. 2004) Arp 220 ($L_{FeHe\alpha} = (1.2 \pm 0.6) \times 10^{40}\,\mathrm{erg\,s^{-1}}$, Iwasawa et al. 2005) and Mrk 273 ($L_{FeHe\alpha} = (9.9^{+8.6}_{-8.1}) \times 10^{40}\,\mathrm{erg\,s^{-1}}$, Balestra et al. 2005). We will use the $\lambda = 8 - 1000\,\mu m$ IR luminosities of these galaxies, taken from the data in Sanders et al. (2003), as proxies for the star formation rate $\mathcal{S}$, making no correction for the fraction of the IR luminosity contributed by any AGN. The $L_{FeHe\alpha}$ luminosities given above are based on the 6.7 keV line photon fluxes quoted in the appropriate paper and scaled to the adopted distances given below.

Weaver et al. (2002) found that the hard X-ray emission in NGC 253 (D=2.6 Mpc, $L_{IR} = 1.9 \times 10^{10}\,L_\odot$) comes from a 300 pc by 60 pc region associated with the nuclear starburst region and gas torus. If we interpret this as a disk of that diameter and height then the equivalent 1-dimensional effective radius is $R_\star = 126$ pc. Scaling M82's observed Fe Heα emission by $(\mathcal{S}_{NGC253}/\mathcal{S}_{M82})^2 \times (R_{\star,M82}/R_{\star,NGC253})$ we obtain a predicted Fe Heα luminosity associated with the starburst of $L_{FeHe\alpha} \sim 4.4 \times 10^{37}\,\mathrm{erg\,s^{-1}}$, which is consistent with the observed value given above.

Arp 299 (D=48.5 Mpc) is a merging system with a total IR luminosity of $L_{IR} = 7.7 \times 10^{11}\,L_\odot$, although the Fe He$\alpha$ emission is only associated with the eastern nucleus (IC 694). Arp 220 (D=74 Mpc) and Mrk 273 (D=158 Mpc) have comparable IR luminosities of $L_{IR} = 1.3 \times 10^{12}\,L_\odot$. As the sizes and geometries of the starburst regions in these galaxies are not well established we will ignore the $R_\star$ scaling and scale the observed M82 Fe Heα luminosity only by the square of the ratio of the IR luminosities. For Arp 299 the predicted Fe Heα luminosity is $L_{FeHe\alpha} \sim 3.0 \times 10^{40}\,\mathrm{erg\,s^{-1}}$, a few times higher than the observed value of $\sim 10^{40}\,\mathrm{erg\,s^{-1}}$. For Arp 220 and Mrk 273 the predicted luminosity is $L_{FeHe\alpha} \sim 8.5 \times 10^{40}\,\mathrm{erg\,s^{-1}}$. This value is comparable to the (poorly-constrained) Fe Heα luminosity of Mrk 273, and several times larger than the observed Fe Heα luminosity of Arp 220. As we would expect the effective size of the starburst regions in these objects to be larger than that of M82 we would expect the luminosity to somewhat less than the predictions given above, so these predictions are in reasonable agreement with the observations.

Such back of the envelope calculations certainly do not prove that the Fe Heα emission seen in these objects arises from the same processes as in M82. They do demonstrate that there is some hope of being able to test and explore this model in objects other than M82 with current X-ray data from the *Chandra* and *XMM-Newton* X-ray Observatories.

In the longer term the superior spectral resolution and sensitivity of the calorimeter instrument on the International X-ray Observatory will allow routine detection of hard X-ray line emission from a much larger sample of star forming galaxies. Furthermore, with an energy resolution of $\Delta E \sim 4$ eV at $E = 6.7$ keV it will allow us to test the assumption that these

lines arise in collisionally heated gas.

6. CONCLUSIONS

We have measured the net energy efficiency of supernova and stellar wind feedback (the thermalization efficiency ϵ) in the starburst galaxy M82 and the degree of central mass-loading β of its superwind by comparing a large suite of 1 and 2-dimensional hydrodynamical models to a set of observational constraints derived from hard X-ray observations of the starburst region (the fluxes of the Heα and Lyα-like lines of S, Ar, Ca and Fe, along with the total diffuse $E = 2 - 8$ keV X-ray luminosity).

The observational constraints are based on a combination of the best currently available observations of the central 500 pc of M82 with both the *Chandra* and *XMM-Newton* X-ray Observatories. We combine the results presented in Strickland & Heckman (2007) on the diffuse hard X-ray Fe line emission and the diffuse $E = 2 - 8$ keV hard X-ray luminosity with new results (this paper) on the S, Ar and Ca lines. By simultaneously applying a large number of observational constraints (we used eight different line fluxes or upper limits, an upper limit on the broad-band X-ray luminosity and a physical requirement that the flow not be strongly radiative) to the simulated starbursts we have been able to constrain the physical properties of the starburst region more tightly than by using more standard X-ray diagnostics.

We modeled the physical properties of the SN-heated and enriched plasma within an assumed disk-like starburst region and the flow of gas outside this region out to a radius of 500 pc using either an appropriately scaled version of the 1-dimensional Chevalier & Clegg (1985) analytical superwind solution, or with a full hydrodynamical simulation using the VH-1 hydrodynamics code in 2-dimensional cylindrical symmetry. We demonstrated a method for correcting the 1-dimensional radial CC model so as to apply to a disk-like starburst geometry with reasonable accuracy. Although this introduces errors of $\lesssim 30\%$ in the individual predicted hard X-ray line fluxes compared to the full 2-D hydrodynamical solution, such errors have little effect on the derived constraints on ϵ and β as the uncertainties in the observed line fluxes can be larger than this. We also considered the issue of the applicability of the adiabatic CC wind solution and find that for the study of the volume-filling gaseous component of the M82 superwind within individual star clusters and over the starburst region as a whole the use of adiabatic models is valid.

We considered a broad range of plausible parameters for the M82 starburst, varying the age and mode of star formation, the starburst region size and geometry, and supernova metal yields. We further considered a correction accounting for the fraction of massive stars that occur in high density regions where high radiative energy losses will preclude their making any contribution to the superwind, which we term the participation fraction ζ.

We find that over all these varied input parameters (we calculated 663 full hydrodynamical simulations using different model parameters, and 4615 models using the scaled CC model), those models that do satisfy the existing observational constraints all have medium to high SN+SW thermalization efficiencies ($30\% \leq \epsilon \leq 100\%$) and have mildly centrally mass-loaded wind fluids (generally $1.5 \leq \beta \leq 2.5$, although in a few cases $\beta = 1$ is allowed).

Our results are ultimately based on the measured Fe Heα emission of the SN heated and enriched plasma driving M82's wind. As such they represent the first direct measurement of the efficiency of SN feedback and mass-loading of the wind fluid in a starburst galaxy. Future observations with higher spectral resolution (e.g. with *ASTRO-H* and *IXO*) will be required to test whether the observed line emission truly arises from a collisional plasma in or close to ionization equilibrium.

That the majority of the models that successfully match our imposed hard X-ray observational constraints also predict thermal pressures in the starburst region ($7.0 \lesssim \log P_{\mathrm{c}}/k \lesssim 7.5$) that are consistent with prior independent estimates of the starburst region pressure increases our confidence in the validity of our method and results.

The allowed values of the SN and SW thermalization efficiency and the mass loading factor correspond to a temperature for the metal-enriched plasma within the starburst region of $30 - 80$ million Kelvin, a mass flow rate of the wind fluid out of the starburst region of $\dot{M}_{\mathrm{tot}} \sim 1.4 - 3.6 \, M_\odot \, \mathrm{yr}^{-1}$ and imply a terminal velocity of the wind (in free expansion) in the range $v_\infty = 1410 - 2240 \, \mathrm{km \, s}^{-1}$. This velocity is considerably larger than the gravitational escape velocity from M82 ($v_{\mathrm{esc}} \lesssim 460 \, \mathrm{km \, s}^{-1}$) and the velocity of the Hα emitting clumps and filaments in the inner 2 kpc of M82's wind ($v_{\mathrm{H}\alpha} \sim 600 \, \mathrm{km \, s}^{-1}$). Reducing the velocity of the wind fluid once *outside* the starburst region to the escape velocity would require either unrealistically large mass loading ($\dot{M}_{\mathrm{extra}} \sim 13 - 240 \, M_\odot \, \mathrm{yr}^{-1}$) or excessive energy losses ($\sim 90 - 98\%$) that must also avoid raising the luminosity of the wind. Thus the hot gas driving M82's wind will probably escape the galaxy's potential well. This result also adds support to the idea that the long term fate of gas within superwinds is phase-dependent.

We show that the luminosity of the hard X-ray line emission produced by the wind fluid in a starburst region scales with the star formation rate $\mathcal{S}$ and starburst size $R_\star$ as $L_{\mathrm{HX}} \propto \mathcal{S}^2/R_\star$. This should serve to distinguish this emission from the other sources of both soft and hard X-ray emission in star forming galaxies that scale linearly with the star formation rate. We show that existing measurements of Fe Heα emission from other actively actively star-forming galaxies (NGC 253, Arp 299, Arp 220, Mrk 273), previously interpreted as ionized reflection from their AGN, are also consistent with our prediction for the wind fluid given the existing observational uncertainties.

Drawing on our results for M82 we have also presented a simple prescription for implementing starburst-driven superwinds in cosmological models of galaxy formation and evolution that more accurately represents the energetics of the hot metal-enriched phases than do existing recipes in the literature.

APPENDIX

A. THE CONDITIONS UNDER WHICH THE ADIABATIC SOLUTION BECOMES INVALID

The basic adiabatic CC model is a function of only three parameters: $\dot{E}_{\rm tot}$, $\dot{M}_{\rm tot}$, and $R_\star$. Silich et al. (2004) were the first to point out that for certain values of these parameters, in particular small $R_\star$ and/or high $\dot{M}_{\rm tot}$, the total luminosity predicted by the CC model was comparable to the net energy injection rate and that the analytical CC solution was no longer self-consistent as it assumed energy losses to be negligible. They developed a self-consistent radiative solution, later tested with numerical hydrodynamical simulations (Tenorio-Tagle et al. 2007).

There in not an exact and easily evaluated function that may be used to assess whether the adiabatic assumption is valid for any particular combination of $\dot{E}_{\rm tot}$, $\dot{M}_{\rm tot}$, and $R_\star$. Nevertheless, Silich et al. (2004) state that the threshold between the adiabatic and the fully radiative solution occurs when the radiative energy losses per unit volume exceed $\sim 30\%$ of the energy injection rate per unit volume. Tenorio-Tagle et al. (2007) show that this is most likely to occur at the very center of the star cluster or starburst region.

In terms of the variables defined in § 3, the adiabatic solution becomes invalid when

$$\frac{\chi_{\rm H}(1+\chi_{\rm H})\rho_{\rm c}^2\,\Lambda(T_{\rm c,Z_{WF}})}{2m_{\rm H}^2} \gtrsim \frac{0.3\,\dot{E}_{\rm tot}}{V_\star}. \tag{A1}$$

Equivalently, if

$$\frac{0.74\,\zeta\,\beta^3\,\dot{M}_{\rm SN+SW}^3\,\Lambda(T_{\rm c,Z_{WF}})}{m_{\rm H}^2\,\epsilon^2\,\dot{E}_{\rm SN+SW}^2\,R_\star} \gtrsim 1 \tag{A2}$$

then radiative losses are high and the CC model is invalid. Note the strong dependence on the mass injection rate and any mass loading, and inverse dependence on the energy injection rate, thermalization efficiency and effective radius. The higher the mean energy per particle, or the larger the starbursting region is, the less-likely significant radiative losses become.

A.1. *Individual star clusters*

Silich et al. (2004) and Tenorio-Tagle et al. (2007) provide examples of star clusters with properties such that radiative losses are severe. However, the mass and energy injection rates they generally use have significantly lower values of the energy per particle (and hence higher radiative losses for a given assumed metal abundance) than what we consider appropriate for clusters in a M82-like starburst.

Equation A2 may be rewritten as an explicit function of the cluster mass. We rewrite the energy and mass injection rates as a function of the star cluster mass assuming in this case an instantaneous starburst model, such that $\dot{E}_{\rm SN+SW} = jM_6$ and $\dot{M}_{\rm SN+SW} = kM_6$, where M_6 is the total cluster mass in units of $10^6\,M_\odot$ (again using a Salpeter IMF between the lower and upper mass limits of $1-100\,M_\odot$). Note that the value of j and k are a functions of the age of the cluster, and are largest in magnitude for a cluster age of $t \sim 4$ Myr in the Starburst99 models. The critical cluster mass above which cooling exceeds 30% of the energy injection and the CC model is no longer valid is then

$$M_6 \gtrsim \frac{m_{\rm H}^2\,\epsilon_{\rm cl}^2\,j^2\,R_{\star,\rm cl}}{0.74\,\zeta_{\rm cl}\,\beta_{\rm cl}^3 k^3\,\Lambda(T,Z_{\rm WF})}. \tag{A3}$$

For the purposes of illustration we consider a cluster of age $t = 5$ Myr, for which $jM_6 = 3.7 \times 10^{40}\,{\rm erg\,s}^{-1}$ and $kM_6 = 2.3 \times 10^{-2}\,M_\odot\,{\rm yr}^{-1}$. For unit ϵ, β, and ζ the central temperature in the CC model would be $T_c \sim 7.5 \times 10^7\,{\rm K}$ (equivalent to $v_\infty = 2250\,{\rm km\,s}^{-1}$). Assuming $Z_{\rm SN+SW} = 5\,Z_\odot$ the cooling function is $\Lambda(T,Z_{\rm WF}) = 5.54 \times 10^{-23}\,{\rm erg\,cm}^3\,{\rm s}^{-1}$.

The massive star clusters observed by McCrady & Graham (2007) in the nuclear starburst region of M82 have half-light radii of between $1-3$ pc. We adopt a typical cluster radius of $R_{\star,\rm cl} = 2$ pc. Substituting these values into Equation A3 we find

$$M_6 \gtrsim 1.9 \times 10^2\,\frac{\epsilon_{\rm cl}^2}{\zeta_{\rm cl}\,\beta_{\rm cl}^3}\left(\frac{5.54 \times 10^{-23}}{\Lambda(T,Z_{\rm WF})}\right)\left(\frac{R_{\star,\rm cl}}{2\,{\rm pc}}\right). \tag{A4}$$

For unit thermalization efficiency and no additional mass loading then no realistic cluster will lie in the radiative regime. Significant mass loading within the cluster (e.g. $\beta_{\rm cl} = 5$) or low thermalization efficiency ($\epsilon_{\rm cl} = 0.1$) are required to reduce M_6 to of order unity for a $t = 5$ Myr old cluster.

An older cluster is even less likely to be radiative. From the Starburst99 models we find that at an age of 20 Myr the mass injection from stellar winds has declined dramatically yielding a net mass injection rate a factor 5 lower than at an age of 5 Myr. The energy injection rate is also lower, but only by a 2.5. At this age even clusters of mass a few times $10^7\,M_\odot$ are still adiabatic even if $\beta_{\rm cl} = 5$ or $\epsilon_{\rm cl} = 0.1$.

A.2. *Starburst regions as a whole*

We rewrite the energy and mass injection rates as a function of the star formation rate $\mathcal{S}$, so that $\dot{E}_{\rm SN+SW} = a\mathcal{S}$ and $\dot{M}_{\rm SN+SW} = b\mathcal{S}$. If we use the values given in Table 4 for constant star formation with an age of 30 Myr, again assuming a metal abundance of $Z_{\rm SN+SW} = 5\,Z_\odot$, we find that the star formation rate must exceed

$$\mathcal{S} \gtrsim 1.4 \times 10^3\,\frac{\epsilon^2}{\zeta\,\beta^3}\left(\frac{5.85 \times 10^{-23}}{\Lambda(T,Z_{\rm WF})}\right)\left(\frac{R_\star}{100\,{\rm pc}}\right). \tag{A5}$$
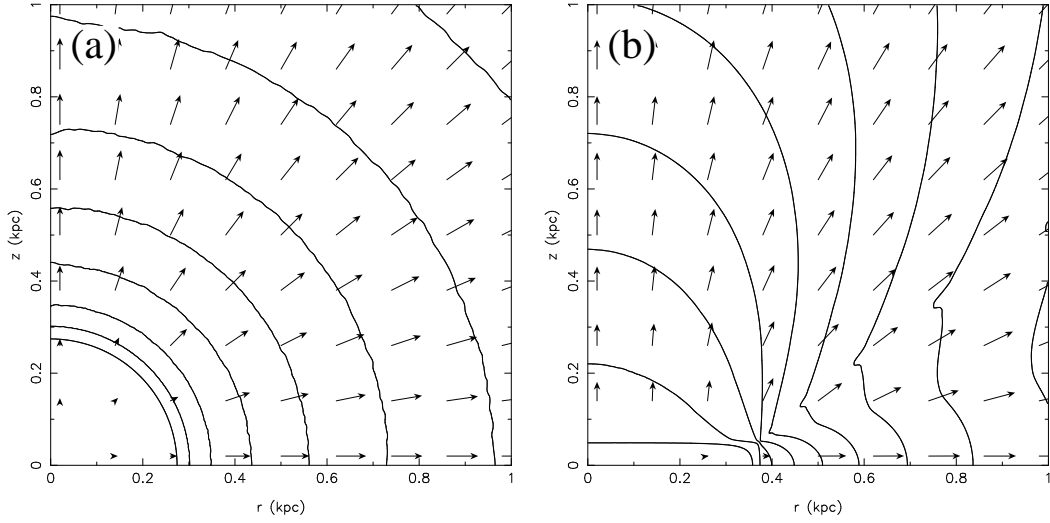
Fig. 12.— Gas number density and velocity vectors in two hydrodynamical simulations of a starburst in (a) a spherical starburst of radius $R_\star = 300$ pc and (b) a disk-like starburst with radius $r_\star = 375$ pc and total thickness $h_\star = 105$ pc. The central gas density and pressure is the same for these configurations. The highest density contour shown corresponds to $\log n = -1.00$ and further contours correspond to successive decreases in $\log n$ in steps of 0.25.

before the adiabatic CC solution becomes invalid.

For M82 the star formation rate is $\mathcal{S} \sim 4 - 6\,M_\odot\,\mathrm{yr}^{-1}$ for the Salpeter IMF assumed, and the starburst region has effective radius of $R_\star \sim 100$ pc at smallest (and more likely $R_\star \sim 300$ pc). Thus the CC model is valid unless mass loading is significant $\beta \gtrsim 5$) or thermalization is inefficient $\epsilon \lesssim 0.1$, or some combination of the two. Note that a low value for the participation fraction ζ will reduce the tendency of the starburst region to be radiative.

We conclude that under most, but not all, conditions the adiabatic Chevalier & Clegg (1985) model is appropriate for M82's nuclear starburst.

B. CORRECTIONS TO THE CC MODEL DUE TO A NON-SPHERICAL STARBURST REGION

It is possible to use the spherical analytical CC model to predict the wind-fluid properties and emission from a disk-like starburst of diameter $d_\star$ and total height $h_\star$ by applying modest numerical corrections that are a fixed function of the geometry alone. As long as the adiabatic assumption is valid these correction factors do not depend on the starburst energy or mass injection rates, and are thus independent of the thermalization efficiency ϵ and the mass loading factor β.

In the analytical CC model the surface area of the starburst region $S_\star$ controls the gas density within the starburst region by limiting the rate at which matter can flow out of it, as described in § 3.2 (see in particular Equ. 30 of Cantó et al. 2000). Note that other parameters, in particular the central temperature and the terminal velocity of the wind are independent of the starburst geometry. Thus, for a given fixed energy and mass injection rate, the central density and pressure in a disk-like starburst of surface area $S_\star = \pi d_\star (d_\star/2 + h_\star)$ should be very similar or identical to values in a spherical starburst of the same surface area $S_\star$.

We tested whether this is indeed the case using the VH-1 hydrodynamical code run in 2-D cylindrical symmetry as described in § 3.1. This code reproduces the standard spherical CC solution to within an accuracy of 0.1% for an assumed spherical starburst. For a disk-like starburst of diameter $d_\star = 750$ pc and $h_\star = 105$ pc (§ 3.3.2) a spherical starburst of equivalent surface area has $R_\star = 300$ pc.

We find that the central density and pressure predicted by VH-1 for this disk-like starburst geometry differs from the values it predicts for a $R_\star = 300$ pc spherical starburst by only 3.1%. Adopting another disk-like geometry with the same surface area ($d_\star = 682$ pc and $h_\star = 200$ pc) yields central density and pressures within 4.2% of the spherical solution. For the other disk-like starburst geometry suggested by observations of M82, with $d_\star = 1015$ pc and $h_\star = 140$ pc the 2-D simulations predict central densities and pressures within 3.7% of the spherical starburst with equivalent surface area ($R_\star = 405$ pc). These simulations demonstrate that we can accurately predict the gas properties *within* a disk-like starburst region using the spherical CC model of equivalent starburst surface area.

The flow pattern exterior to the starburst region is also influenced by the geometry of the starburst region. A disk with $d_\star > h_\star$ will weakly collimate the flow along the minor axis and give the superwind a preferred direction even in the absence of external collimation by the ISM. In Fig. 12 we illustrate this by plotting the density and velocity fields for equivalent spherical and disk-like starbursts.

For our purposes the main effect is that the resulting non-spherical flow alters the total volume emission integral within any fixed region that is larger than the starburst region. Within the starburst region itself this effect is not particularly significant when evaluating total gas masses or emission integral given the relative uniformity of the density and pressure. However, outside and above a disk-like starburst region the gas density drops off with increasing height more slowly that the $\rho \propto R^{-2}$ predicted by the CC model.

Calculating the correct emission integral for a disk-like starburst based the results of the spherical CC model thus entails some geometry-based corrections because of the different starburst region volumes and secondly due to the non-spherical flow pattern outside the starburst region. The first correction is trivial to evaluate analytically. The second correction must be determined from

a full hydrodynamical simulation of the specific disk-like starburst, and further depends on the size of region R_{obs} we wish to evaluate the emission integral over.

Our procedure for calculating the gas properties and total emission of disk-like starburst regions using the spherical CC model is as follows:

1. For a given starburst geometry evaluate the surface area $S_\star$, and run a simulation using the CC model using the effective starburst radius $R_\star = (S_\star/4\pi)^{1/2}$. This accurately predicts the values of fluid variables such as density, temperature and pressure *within* the starburst region.

2. Macroscopic variables, in particular the volume emission integral, require further geometrical corrections to make the emission integral predicted using the spherical CC model, EI_{CC}, match the emission integral found in a full multi-dimensional simulation of a non-spherical starburst region EI_{nonsph}.

3. The volume of the starburst region in the spherical model is larger than the volume of the disk-like starburst region, so the volume emission integral predicted by the CC model within some radius $R_{obs} \geq R_\star$ must be scaled by a factor K_V equal to the ratio of the starburst region volumes:

$$K_V = \frac{\pi r_\star^2 h_\star}{(4\pi/3)R_\star^3}. \tag{B1}$$

4. A full hydrodynamical simulation for a given disk-like starburst must be run to evaluate the correction $K_{nonsph} = EI_{nonsph}/(K_V\,EI_{CC})$ to the emission integral within the chosen R_{obs} due to the non-spherical flow pattern manifest outside the starburst region. We use $R_{obs} = 500$ pc to match the region from which the M82 nuclear region spectra analyzed in Paper I were extracted. Simulations of different disk-like starburst regions where we altered the thermalization efficiency and mass loading demonstrated that the correction K_{nonsph} to the total emission integral is a fixed function of the geometry, and is independent of the energy and mass injection rates.

5. The temperature-dependent differential emission measure for the scaled CC model $EI_{SCC}(T)$ is calculated using the factors discussed above: $EI_{SCC}(T) = K_V \times K_{nonsph} \times EI^{CC}(T)$. Combining this with the temperature-dependent cooling functions and summing over all temperatures gives the final predicted luminosity for the chosen energy band or line.

For $R_{obs} = 500$ pc and a disk-like starburst with $d_\star = 750$ pc and $h_\star = 105$ pc, the primary geometry we apply to M82, the non-spherical emission integral correction factor $K_{nonsph} = 1.64$. For the alternate disk-like starburst geometry with $d_\star = 1015$ pc and $h_\star = 140$ pc the correction factor is $K_{nonsph} = 1.52$. For the compact starbursting disk with $d_\star = 300$ pc and $h_\star = 60$ pc the correction factor is $K_{nonsph} = 1.59$.

With these scalings the spherical CC model can be used to predict to high accuracy the total emission integral from the wind fluid within R_{obs} for a disk-like starburst. This method is less accurate at reproducing the luminosity predicted by a full 2-dimensional hydrodynamical simulation because non-spherical flow pattern leads to subtle differences in the shape of the differential emission integral EI(T) compared to a spherical CC solution.

We compared the luminosities predicted by a small suite of hydrodynamical models with different disk-like starburst geometries to the results from the scaled CC analytical model in order to assess the significance of this effect. The error introduced by the effect is small in terms of computing the total cooling rate ($< 2\%$ for the Sutherland & Dopita cooling curve), or even the the X-ray luminosity over the broad $0.3 - 2.0$ keV or $2 - 8$ keV energy ranges ($\lesssim 10\%$). For the high energy lines we are interested in because of their temperature sensitivity the effect is larger, and the associated errors in predicted line luminosity can be as large as $\sim 30\%$.

Nevertheless these uncertainties do not compromise the usefulness of the scaled CC model as they are comparable to the observational uncertainties in the nuclear region S, Ar and Ca luminosities of the well detected lines from the *XMM-Newton* data, and less than the uncertainties in the diffuse Fe Heα line luminosity derived from the *Chandra* ACIS-S data. The relative effect of these uncertainties on the region of model parameter space matching our chosen constraints can be seen in Fig. 7.

C. ESTIMATING THE PARTICIPATION FRACTION ζ

There are two main environments that in principle might reduce the fraction ζ of all the SNe and stellar winds in a starburst region that can contribute to powering a superwind. The first, likely to to be the most significant but also hardest to estimate, is physical confinement and increased radiative cooling of young supernova remnants and stellar winds occurring in regions of high ambient gas density such as molecular clouds. The second is that radiative losses may be high for those SNe and stellar winds associated with massive stars in massive and compact star clusters (particularly super star clusters), where the adiabatic CC solution is no longer valid.

There are some observational findings that are suggest that some fraction of the SNe in M82's nuclear starburst occurred within regions of gas number density $n \gtrsim 10^3$ cm^{-3} (Kronberg et al. 2000; Chevalier & Fransson 2001; Seaquist & Stanković 2007), although there are problems with this interpretation (see Beswick et al. 2006, and references therein). However, based on the total molecular gas mass of $\sim 10^8\,M_\odot$ within the starburst region, the fraction of the total starburst region volume occupied by such dense gas must be $\eta \lesssim 0.1$ or lower (Lugten et al. 1986; Nakai et al. 1987). Massive stars will be born in regions of high gas density, so that if confinement does occur the magnitude of the drop in ζ may well be larger the the filling factor of the dense gas. At present we can not rigorously quantify the effectiveness of confinement, nor the fraction of stars that might be affected. Chevalier & Fransson (2001) speculate that perhaps as much as 50% of the SNe in M82 occur in dense regions, in which case the participation factor may be as low as $\zeta \sim 0.5$.

It is possible to quantitatively estimate the role that over-cooling of the thermalized SN and stellar wind ejecta in dense star clusters have on ζ. Based on the discussion in Appendix A we conclude that only the compact clusters of radii a few parsecs and masses $M_{\rm rad} \gtrsim 10^6\,M_\odot$ (Salpeter IMF, mass limits $1-100\,M_\odot$) are likely to suffer significant radiative losses (and then only under certain conditions).

For a star cluster mass function of the form $dN_{\rm cl} \propto M_{\rm cl}^{-\gamma}\,dM$ between the mass limits $M_{\rm cl,min}$ and $M_{\rm cl,max}$ and where $\gamma = 2$ (Weidner & Kroupa 2006), the fraction of the total stellar mass in clusters with $M_{\rm cl} \gtrsim M_{\rm rad}$ is

$$f = \frac{\ln M_{\rm cl,max} - \ln M_{\rm rad}}{\ln M_{\rm cl,max} - \ln M_{\rm min}}. \tag{C1}$$

We adopt a minimum cluster mass of $M_{\rm cl,min} = 5\,M_\odot$ and a maximum cluster mass of $M_{\rm cl,max} = 10^7\,M_\odot$ (Weidner et al. 2004). For $M_{\rm rad} = 10^6\,M_\odot$ then $f = 0.16$. Thus the magnitude of the reduction in ζ due to radiative cluster winds is small, of order 15%, even if SN and stellar wind thermalization is inefficient, and/or there are long-lived sources of additional mass loading in the massive star clusters.

REFERENCES

Achtermann, J. M. & Lacy, J. H. 1995, ApJ, 439, 163
Adelberger, K. L., Steidel, C. C., Shapley, A. E., & Pettini, M. 2003, ApJ, 584, 45
Anders, E. & Grevesse, N. 1989, Geochim. Cosmochim. Acta, 53, 197
Arnaud, K. A. 1996, in Astronomical Society of the Pacific Conference Series, Vol. 101, Astronomical Data Analysis Software and Systems V, ed. G. H. Jacoby & J. Barnes, 17
Balestra, I., Boller, T., Gallo, L., Lutz, D., & Hess, S. 2005, A&A, 442, 469
Ballo, L., Braito, V., Della Ceca, R., Maraschi, L., Tavecchio, F., & Dadina, M. 2004, ApJ, 600, 634
Bertone, S., Stoehr, F., & White, S. D. M. 2005, MNRAS, 359, 1201
Beswick, R. J., Riley, J. D., Marti-Vidal, I., Pedlar, A., Muxlow, T. W. B., McDonald, A. R., Wills, K. A., Fenech, D., & Argo, M. K. 2006, MNRAS, 369, 1221
Bland-Hawthorn, J. 1995, **??**jnlPASA, 12, 190
Blondin, J. M., Kallman, T. R., Fryxell, B. A., & Taam, R. E. 1990, ApJ, 356, 591
Calzetti, D., Harris, J., Gallagher, III, J. S., Smith, D. A., Conselice, C. J., Homeier, N., & Kewley, L. 2004, AJ, 127, 1405
Cantó, J., Raga, A. C., & Rodríguez, L. F. 2000, ApJ, 536, 896
Cen, R. & Fang, T. 2006, ApJ, 650, 573
Cen, R., Nagamine, K., & Ostriker, J. P. 2005, ApJ, 635, 86
Cen, R. & Ostriker, J. P. 2006, ApJ, 650, 560
Chandar, R., Leitherer, C., Tremonti, C. A., Calzetti, D., Aloisi, A., Meurer, G. R., & de Mello, D. 2005, ApJ, 628, 210
Chevalier, R. A. & Clegg, A. W. 1985, Nature, 317, 44
Chevalier, R. A. & Fransson, C. 2001, ApJ, 558, L27
Colbert, E. J. M., Heckman, T. M., Ptak, A. F., Strickland, D. K., & Weaver, K. A. 2004, ApJ, 602, 231
Cooper, J. L., Bicknell, G. V., Sutherland, R. S., & Bland-Hawthorn, J. 2008, ApJ, 674, 157
Dahlem, M. 1997, PASP, 109, 1298
Dahlem, M., Lisenfeld, U., & Rossa, J. 2006, A&A, 457, 121
de Grijs, R. 2001, Astronomy and Geophysics, 42, 12
de Grijs, R., O'Connell, R. W., & Gallagher, III, J. S. 2001, AJ, 121, 768
de Grijs, R. & Parmentier, G. 2007, Chinese Journal of Astronomy and Astrophysics, 7, 155
Devine, D. & Bally, J. 1999, ApJ, 510, 197
Dogiel, V. A., Inoue, H., Masai, K., Schönfelder, V., & Strong, A. W. 2002, ApJ, 581, 1061
Dyson, J. E., Hartquist, T. W., & Biro, S. 1993, MNRAS, 261, 430
Efstathiou, G. 2000, MNRAS, 317, 697
Förster Schreiber, N. M., Genzel, R., Lutz, D., & Sternberg, A. 2003a, ApJ, 599, 193
Förster Schreiber, N. M., Sauvage, M., Charmandaris, V., Laurent, O., Gallais, P., Mirabel, I. F., & Vigroux, L. 2003b, A&A, 399, 833
Garnett, D. R. 2002, ApJ, 581, 1019
Gibson, B. K., Loewenstein, M., & Mushotzky, R. F. 1997, MNRAS, 290, 623
Götz, M., Downes, D., Greve, A., & McKeith, C. D. 1990, A&A, 240, 52
Griffiths, R. E. et al. 2000, Science, 290, 1325
Grimes, J. P., Heckman, T., Strickland, D., Dixon, W. V., Sembach, K., Overzier, R., Hoopes, C., Aloisi, A., & Ptak, A. 2007, ApJ, 668, 891
Grimm, H.-J., Gilfanov, M., & Sunyaev, R. 2003, MNRAS, 339, 793
Heckman, T. M. 2003, in Galaxy Evolution: Theory & Observations, ed. V. Avila-Reese, C. Firmani, C. S. Frenk, & C. Allen (Revista Mexicana de Astronomía y Astrofísica Conference Series 17), 47
Heckman, T. M., Armus, L., & Miley, G. K. 1990, ApJS, 74, 833
Heckman, T. M., Lehnert, M. D., Strickland, D. K., & Armus, L. 2000, ApJS, 129, 493
Heckman, T. M., Sembach, K. R., Meurer, G. R., Strickland, D. K., Martin, C. L., Calzetti, D., & Leitherer, C. 2001, ApJ, 554, 1021
Hoopes, C. G., Heckman, T. M., Strickland, D. K., & Howk, J. C. 2003, ApJ, 596, L175
Inui, T., Matsumoto, H., Tsuru, T. G., Koyama, K., Matsushita, S., Peck, A. B., & Tarchi, A. 2005, PASJ, 57, 135

Iwasawa, K., Sanders, D. B., Evans, A. S., Trentham, N., Miniutti, G., & Spoon, H. W. W. 2005, MNRAS, 357, 565
Jenkins, L. P., Roberts, T. P., Ward, M. J., & Zezas, A. 2004, MNRAS, 352, 1335
Ji, L., Wang, Q. D., & Kwan, J. 2006, MNRAS, 372, 497
Kennicutt, R. C. 1998, ARA&A, 36, 189
Kobayashi, C., Springel, V., & White, S. D. M. 2007, MNRAS, 376, 1465
Kronberg, P. P., Biermann, P., & Schwab, F. R. 1985, ApJ, 291, 693
Kronberg, P. P., Sramek, R. A., Birk, G. T., Dufton, Q. W., Clarke, T. E., & Allen, M. L. 2000, ApJ, 535, 706
Kroupa, P. 2001, MNRAS, 322, 231
Larson, R. B. 1974, MNRAS, 169, 229
Lehnert, M. D. & Heckman, T. M. 1996a, ApJ, 462, 651
—. 1996b, ApJ, 472, 546
Lehnert, M. D., Heckman, T. M., & Weaver, K. A. 1999, ApJ, 523, 575
Leitherer, C. & Heckman, T. M. 1995, ApJS, 96, 9
Leitherer, C., Robert, C., & Drissen, L. 1992, ApJ, 401, 596
Leitherer, C. et al. 1999, ApJS, 123, 3
Limongi, M. & Chieffi, A. 2007, in American Institute of Physics Conference Series, Vol. 924, The Multicolored Landscape of Compact Objects and Their Explosive Origins, ed. T. di Salvo, G. L. Israel, L. Piersant, L. Burderi, G. Matt, A. Tornambe, & M. T. Menna, 226–233
Lira, P., Ward, M., Zezas, A., Alonso-Herrero, A., & Ueno, S. 2002, MNRAS, 330, 259
Lugten, J. B., Watson, D. M., Crawford, M. K., & Genzel, R. 1986, ApJ, 311, L51
Mac Low, M. & McCray, R. 1988, ApJ, 324, 776
Martin, C. L. 1999, ApJ, 513, 156
—. 2005, ApJ, 621, 227
Martin, C. L., Kobulnicky, H. A., & Heckman, T. M. 2002, ApJ, 574, 663
Mas-Hesse, J. M. & Cerviño, M. 1999, in IAU Symposium, Vol. 193, Wolf-Rayet Phenomena in Massive Stars and Starburst Galaxies, ed. K. A. van der Hucht, G. Koenigsberger & P. R. J. Eenens, 550
Masai, K., Dogiel, V. A., Inoue, H., Schönfelder, V., & Strong, A. W. 2002, ApJ, 581, 1071
Mayya, Y. D., Bressan, A., Carrasco, L., & Hernandez-Martinez, L. 2006, ApJ, 649, 172
McCrady, N., Gilbert, A. M., & Graham, J. R. 2003, ApJ, 596, 240
McCrady, N. & Graham, J. R. 2007, ApJ, 663, 844
McKee, C. F. & Ostriker, J. P. 1977, ApJ, 218, 148
McKeith, C. D., Greve, A., Downes, D., & Prada, F. 1995, A&A, 293, 703
Melioli, C. & de Gouveia Dal Pino, E. M. 2004, A&A, 424, 817
Melioli, C., de Gouveia dal Pino, E. M., & Raga, A. 2005, A&A, 443, 495
Melo, V. P., Muñoz-Tuñón, C., Maíz-Apellániz, J., & Tenorio-Tagle, G. 2005, ApJ, 619, 270
Moran, E. C. & Lehnert, M. D. 1997, ApJ, 478, 172
Muxlow, T. W. B., Pedlar, A., Wilkinson, P. N., Axon, D. J., Sanders, E. M., & de Bruyn, A. G. 1994, MNRAS, 266, 455
Nakai, N., Hayashi, M., Handa, T., Sofue, Y., Hasegawa, T., & Sasaki, M. 1987, PASJ, 39, 685
Netzer, H., Lemze, D., Kaspi, S., George, I. M., Turner, T. J., Lutz, D., Boller, T., & Chelouche, D. 2005, ApJ, 629, 739
O'Connell, R. W., Gallagher, J. S., Hunter, D. A., & Colley, W. N. 1995, ApJ, 446, L1
Oppenheimer, B. D. & Davé, R. 2006, MNRAS, 373, 1265
Origlia, L., Ranalli, P., Comastri, A., & Maiolino, R. 2004, ApJ, 606, 862
Oskinova, L. M. 2005, MNRAS, 361, 679
Persic, M. & Rephaeli, Y. 2007, A&A, 463, 481
Pettini, M., Shapley, A. E., Steidel, C. C., Cuby, J., Dickinson, M., Moorwood, A. F. M., Adelberger, K. L., & Giavalisco, M. 2001, ApJ, 554, 981
Ranalli, P., Comastri, A., & Setti, G. 2003, A&A, 399, 39
Ross, R. R. & Fabian, A. C. 2005, MNRAS, 358, 211
Rupke, D. S., Veilleux, S., & Sanders, D. B. 2005, ApJS, 160, 115
Sanders, D. B., Mazzarella, J. M., Kim, D.-C., Surace, J. A., & Soifer, B. T. 2003, AJ, 126, 1607

Satyapal, S., Watson, D. M., Pipher, J. L., Forrest, W. J., Greenhouse, M. A., Smith, H. A., Fischer, J., & Woodward, C. E. 1997, ApJ, 483, 148

Schaaf, R., Pietsch, W., Biermann, P. L., Kronberg, P. P., & Schmutzler, T. 1989, ApJ, 336, 722

Seaquist, E. R. & Stanković, M. 2007, ApJ, 659, 347

Shapley, A. E., Steidel, C. C., Pettini, M., & Adelberger, K. L. 2003, ApJ, 588, 65

Shopbell, P. L. & Bland-Hawthorn, J. 1998, ApJ, 493, 129

Silich, S., Tenorio-Tagle, G., & Añorve-Zeferino, G. A. 2005, ApJ, 635, 1116

Silich, S., Tenorio-Tagle, G., & Rodríguez-González, A. 2004, ApJ, 610, 226

Smith, L. J. & Gallagher, J. S. 2001, MNRAS, 326, 1027

Smith, L. J., Westmoquette, M. S., Gallagher, J. S., O'Connell, R. W., Rosario, D. J., & de Grijs, R. 2006a, MNRAS, 370, 513

Smith, R. K., Brickhouse, N. S., Liedahl, D. A., & Raymond, J. C. 2001, ApJ, 556, L91

Smith, R. K., Dame, T. M., Costantini, E., & Predehl, P. 2006b, ApJ, 648, 452

Sofue, Y. 1998, PASJ, 50, 227

Songaila, A. 1997, ApJ, 490, L1

Springel, V. & Hernquist, L. 2003a, MNRAS, 339, 289

—. 2003b, MNRAS, 339, 312

Steinmetz, M. & Navarro, J. F. 1999, ApJ, 513, 555

Stevens, I. R. & Hartwell, J. M. 2003, MNRAS, 339, 280

Stevens, I. R., Read, A. M., & Bravo-Guerrero, J. 2003, MNRAS, 343, L47

Strickland, D. K. & Heckman, T. M. 2007, ApJ, 658, 258

Strickland, D. K., Heckman, T. M., Colbert, E. J. M., Hoopes, C. G., & Weaver, K. A. 2004a, ApJS, 151, 193

—. 2004b, ApJ, 606, 829

Strickland, D. K., Heckman, T. M., Weaver, K. A., & Dahlem, M. 2000, AJ, 120, 2965

Strickland, D. K., Heckman, T. M., Weaver, K. A., Hoopes, C. G., & Dahlem, M. 2002, ApJ, 568, 689

Strickland, D. K. & Stevens, I. R. 2000, MNRAS, 314, 511

Suchkov, A. A., Balsara, D. S., Heckman, T. M., & Leitherer, C. 1994, ApJ, 430, 511

Suchkov, A. A., Berman, V. G., Heckman, T. M., & Balsara, D. S. 1996, ApJ, 463, 528

Sutherland, R. S. & Dopita, M. A. 1993, ApJS, 88, 253

Tenorio-Tagle, G., Wünsch, R., Silich, S., & Palouš, J. 2007, ApJ, 658, 1196

Thornton, K., Gaudlitz, M., Janka, H.-T., & Steinmetz, M. 1998, ApJ, 500, 95

Tomisaka, K. & Bregman, J. N. 1993, PASJ, 45, 513

Tremonti, C. et al. 2004, ApJ, 613, 989

Tremonti, C. A., Calzetti, D., Leitherer, C., & Heckman, T. M. 2001, ApJ, 555, 322

Veilleux, S., Cecil, G., & Bland-Hawthorn, J. 2005, ARA&A, 43, 769

Weaver, K. A., Heckman, T. M., Strickland, D. K., & Dahlem, M. 2002, ApJ, 576, L19

Weidner, C. & Kroupa, P. 2006, MNRAS, 365, 1333

Weidner, C., Kroupa, P., & Larsen, S. S. 2004, MNRAS, 350, 1503

Westmoquette, M. S., Smith, L. J., Gallagher, III, J. S., O'Connell, R. W., Rosario, D. J., & de Grijs, R. 2007, ApJ, 671, 358

Woosley, S. E. & Weaver, T. A. 1995, ApJS, 101, 181